WHITE PAPER ON MAAT@GTC

Francisco Prada,[1] Robert Content,[2] Ariel Goobar,[3] Luca Izzo,[4] Enrique Pérez,[1] José A. Acosta Pulido,[5] Santiago Arribas,[6] Adriano Agnello,[4] Jose M. Diego,[7] Francisco J. Carrera,[7] Amalia Corral,[7] Lluís Galbany,[8] Jorge García Rojas,[5] David Jones,[5] Jon Lawrence,[2] Eduardo Martín,[5] Silvia Mateo,[7] Silvia Martínez Nuñez,[7] Evencio Mediavilla,[5] M. Ángeles Pérez García,[9] Jorge Sánchez Almeida,[5] Eva Villaver,[10] María Rosa Zapatero Osorio,[6] Fabrizio Arrigoni Battaia,[11] David Barrado,[6] Víctor J. S. Béjar,[5] Henri M. J. Boffin,[12] Hervé Bouy,[13] Adam Burgasser,[14] César Esteban,[5] Nuria Huélamo,[6] Nicolas Lodieu,[5] María Morales Calderón,[6] Antonio Pérez Garrido,[15] Pablo Rodríguez Gil,[5] Miguel Santander García,[5] Enrique Solano,[6] Manuel A. P. Torres,[5] Roger Wesson,[16] and YOU

[1]Instituto de Astrofísica de Andalucía (CSIC), Granada, Spain

[2]Australian Astronomical Optics - Macquarie University, Sidney, Australia

[3]The Oskar Klein Centre for Cosmoparticle Physics, Stockholm University, Sweden

[4]DARK, Niels Bohr Institute, Copenhagen, Denmark

[5]Instituto de Astrofísica de Canarias and Universidad de La Laguna, Tenerife, Spain

[6]Centro de Astrobiología, Madrid, Spain

[7]Instituto de Física de Cantabria (CSIC-UC), Santander, Spain

[8]Departamento de Física Teórica y del Cosmos, Universidad de Granada, Spain

[9]Departamento de Física Fundamental, Universidad de Salamanca, Spain

[10]Departamento de Física Teórica, Universidad Autónoma de Madrid, Spain

[11]Max Planck Institut für Astrophysik, Garching, Germany

[12]European Southern Observatory, Germany

[13]University of Bordeaux, France

[14]University of California San Diego, USA

[15]UPCT, Universidad de Murcia, Spain

[16]University Colleague London, UK

ABSTRACT

MAAT is proposed as a visitor mirror-slicer optical system that will allow the OSIRIS spectrograph on the 10.4 m GTC telescope the capability to perform Integral-Field Spectroscopy (IFS) over a seeing-limited field-of-view $14.20'' \times 10''$ with a slice width of $0.303''$. MAAT@GTC will enhance the resolution power of OSIRIS by 1.6 times with respect to its $0.6''$ wide long-slit. All the eleven OSIRIS grisms and VPHs will be available to provide broad spectral coverage with moderate resolution (R=600 up to 4100) in the $3600-10000$ Å spectral range. MAAT unique observing capabilities will broaden its use to the needs of the GTC community for unveiling the nature of most striking phenomena in the universe well beyond time-domain astronomy. The GTC equipped with OSIRIS+MAAT will also play a fundamental role in synergy with other facilities operating at the northern ORM at La Palma. This White Paper presents the different aspects of MAAT@GTC, including scientific and technical specifications, outstanding science cases and outline of the instrument concept, aiming at first light by the start of 2022.

Corresponding author: Francisco Prada
f.prada@csic.es

Contents

1. MAAT BASIC DESCRIPTION

MAAT[1] (Mirror-slicer Array for Astronomical Transients) is proposed as a new mirror-slicer optical system that will allow the OSIRIS spectrograph at the 10.4-m GTC telescope[2] (see a nice outside / inside view of GTC in Figure 1) the capability to perform integral-field spectroscopy (IFS) over a seeing-limited field of view $14.20'' \times 10.0''$. MAAT will enhance the resolution power of OSIRIS by 1.6 times with respect to its $0.6''$ wide long-slit. All the eleven OSIRIS grisms and volume-phase holographic gratings (VPHs) will be available to provide broad spectral coverage with moderate resolution (R=600 up to 4100) in the spectral range 360-1000 nm. The basic parameters of MAAT@GTC are listed in Table 5).
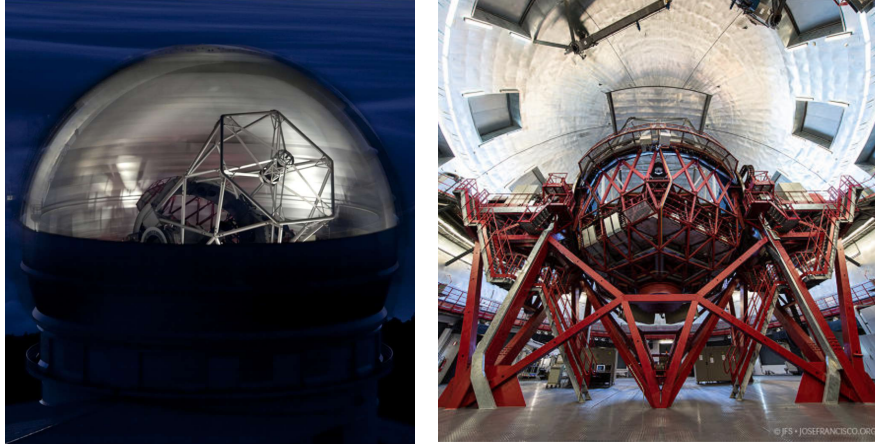

Figure 1. Outside / inside view of the Gran Telescopio CANARIAS (GTC). Credits: ING and *josefrancisco.org*.

The integral-field unit (IFU) consists of an imaging slicer optical system with 33 slices (4 CCD pixels separation between slices) each of $0.303'' \times 14.20''$. Figure 2 shows the sky footprint of the MAAT mirror-slicer IFU. The IFS mode will take advantage of the expected significant increase in the overall OSIRIS efficiency due to its new e2v $4k \times 4k$ detector that will be installed after the relocation of OSIRIS at the Cassegrain focus of GTC. Table 2 compares MAAT with the other existing seeing-limited IFS on 10m-class telescopes located on both hemispheres. In terms of opportunity, of all these systems, MAAT provides the unique capability of a broad-band spectral coverage over the entire spectral range from the UV up to the near-IR (360-1000 nm).

Figure 3 showcases the simulated MAAT view of the galaxy NGC300 (see Section 5 for details). The top-right image zooms in the circumnuclear region of NGC300 (top-left) around the HII region De74 on the left (green as dominated by the [OIII] and Hα emission lines) and the SN remnant S14 on the right (orange as dominated by the shocked [SII] emission lines). The two images below correspond to the HII region De74 and the SN remnant S14 as seen by the slicer. The detector spectral images (Figure 17) show the wealth of emission lines typical of these type of objects; an expanded view around the [OI]6300 to [SII]6731 spectral region includes the bright [OI] Earth atmospheric emission and it clearly shows the presence of [OI] 6300 in the SN remnant but it is conspicuously absent in the HII region.

MAAT is devised as a IFS-mode for OSIRIS devoted to unveiling the nature of most striking phenomena in the universe, see Section 3. Furthermore, MAAT top-level requirements will broaden its use to the needs of the GTC community for a wide range of competitive science topics that covers the entire astronomy given its unique observing capabilities.

2. WHY MAAT ON THE GTC?

Long-slit observations of a point source are affected by the atmosphere at least in two ways: the slit size should be adapted to match the seeing (with the subsequent undesired changes in spectral resolution) and the chromatic atmospheric dispersion spatially shifts and broadens the images depending on the wavelength. Both drawbacks affect to the quality of the observed spectra and often lead to large observing overheads. Integral Field Spectroscopy (IFS)

---

[1] MAAT refers to the ancient Egyptian concepts of truth, balance, order, harmony, law, morality, justice, and cosmic order.
[2] http://www.gtc.iac.es

Table 1. The MAAT basic parameters

Parameter	Value
Spectrograph	OSIRIS at GTC-Cass
Module	Integral Field Unit
Field of View[1]	$14.20'' \times 10.00''$
Field aspect ratio	1.42
Slit width	$0.303''$
Spatial sampling[2]	$0.303'' \times 0.127''$
Wavelength range	360 to 1000 nm
Spectral resolution[3]	600 to 4100
Detector[4]	$4k \times 4k$ (15 μm pixel)
CCD plate scale	$0.127''$ per pixel

[1] IFU surface on the sky is 142 arcsec^2, and 141 arcsec^2 without vignetting).

[2] With 1×2 CCD binning $0.303'' \times 0.254''$.

[3] Enhanced 1.6 times resolving power w.r.t. to that of a $0.6''$ long-slit. All OSIRIS grisms and VPHs can be used.

[4] The new OSIRIS detector is a Teledyne-e2v CCD231-84 deep-depleted standard silicon, astro multi-2.

Table 2. Seeing-limited Integral Field Spectrographs on 10m-class telescopes.

Sky	Telescope	Instrument	Spectral range	Resolution	Field of View	Spatial sampling	IFU
Southern	VLT	MUSE	480-930 nm	1770-3590	$59.9'' \times 60.0''$	$0.2'' \times 0.2''$	mirror slicer
Northern	Keck	KCWI	350–560 nm	3000-4000	$8.25'' \times 20.0''$	$0.34'' \times 0.147''$	mirror slicer
N & S	Gemini	GMOS-IFU	360-940 nm	600-4400	$5.0'' \times 7.0''$	$0.2''$	lenslet/fibers
Northern	**GTC**	**OSIRIS+MAAT**	**360-1000 nm**	**600-4100**	**$10.0'' \times 14.20''$**	**$0.303'' \times 0.127''$**	**mirror slicer**

records simultaneously complete spectral and spatial information of the source, a data cube, which can be corrected from chromatic atmospheric refraction. Consequently, no object acquisition is, basically, needed to obtain high quality spectroscopic data. On the other hand, the possibility of extracting images at constant wavelength allows you to perform spectro-astrometry, a technique to study the structure and kinematics of an astronomical source on scales much smaller than the diffraction limit of the telescope.

Most of the advantages of the IFS technique are direct consequences of the simultaneity when recording spatial and spectral information. The simultaneity not only implies a more efficient way of observing but, more importantly, it guarantees a great homogeneity in the data. In addition, IFS has other advantages. With IFS systems there is no need for an accurate centering of the object in the slit or to adapt the slit width (spectral resolution) to the seeing conditions; neither are the data affected by "slit effects" when determining radial velocities (Vanderriest 1995). Using IFS it is possible to determine and to correct in the spectra the effects of chromatic atmospheric refraction, using an a posteriori procedure. This is obviously important to preserve the spectro-photometric properties of the spectra without
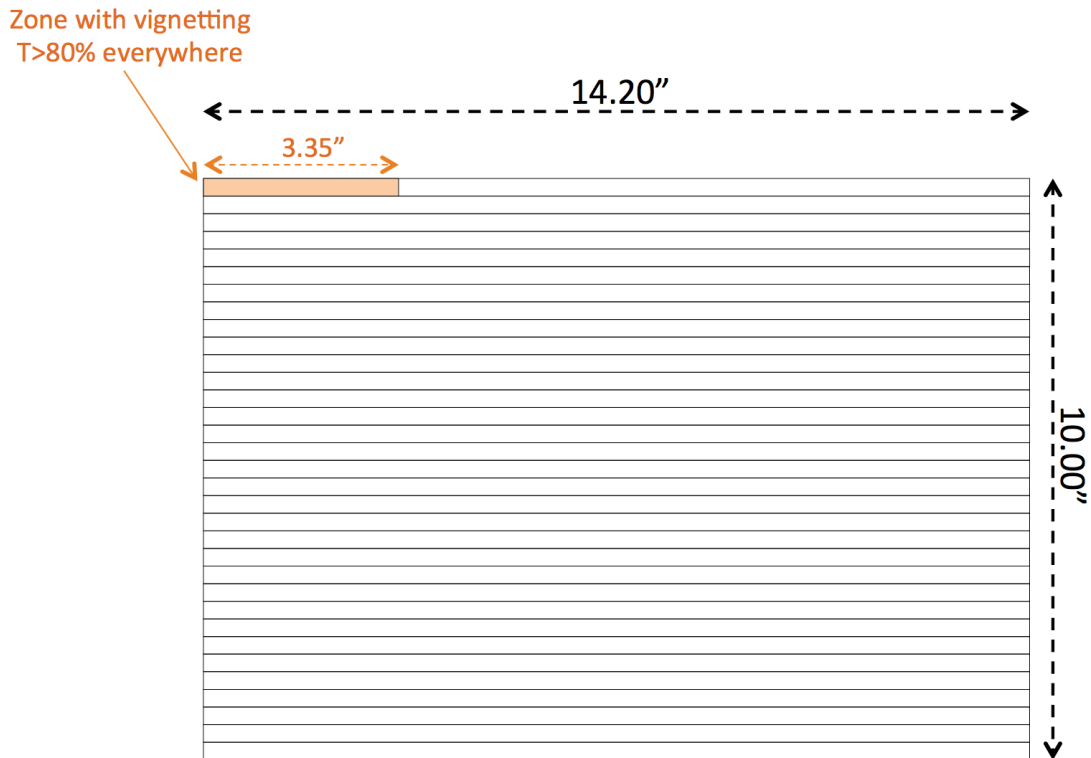
Zone with vignetting
T>80% everywhere

14.20"

3.35"

10.00"

Figure 2. Sky footprint of the MAAT mirror-slicer IFU.

the use of an atmospheric dispersion corrector (ADC). Note that for long-slit observations the presence of chromatic atmospheric refraction imposes strong restrictions, which cannot be corrected by any means. Thus, the slit must be orientated along a direction defined by the parallactic angle (i.e. the spatial direction is predefined) if it is required to preserve the relative fluxes in the spectrum. If the slit is orientated at a desired position angle (no coincident with the one along which the differential atmospheric refraction takes place) special filters for the acquisition / guiding systems should be used to optimize the detection in a particular wavelength range, other spectral ranges being affected by light losses. To have a complete feel for these difficulties, we should note that the effects of differential atmospheric refraction are dynamic, in the sense that they change with time. All these problems are strong drawbacks to obtain high quality spectra, in particular when monitoring of one object at different epochs with different atmospheric conditions is required. In summary, we can say that IFS can be the first choice technique to do spectroscopic monitoring of even point sources.

The idea of measuring the wavelength dependence of the center of an astronomical source to study its structure and kinematics at scales much smaller than the diffraction limit (spectro-astrometry, Bailey (1998)) was initially developed from different experimental grounds (speckel interferometry, broad band photometry, long-slit spectroscopy) and was based in specific and/or iterative observational strategies. This complexity is overtaken by Integral Field Spectroscopy (IFS) that offers a simple way to obtain the spatial distribution of a given spectral feature (see Gnerucci et al. 2010, 2011b,a, for a long-slit vs. IFS comparison).

An example of what can be obtained (without any specific observational strategy or methodological analysis) directly from IFS can be seen in Figure 5 (Arribas et al. 1999)) where the photo-centers of a point-like source at different wavelengths nicely trace chromatic atmospheric refraction with an accuracy better than 5 mas well below the spaxel size (a fiber face of 0.45 arcsec) and below the diffraction limit of the telescope (approx. 40 m.a.s. for the 4.2m WHT telescope). Spectro-astrometry has been used (or suggested its use) to study binaries (Baines et al. 2004) (Porter et al. 2005), disks around stars (Takami et al. 2003; Whelan et al. 2005), supermassive black-holes (Gnerucci et al. 2010, 2011b,a), jets in AGNs, mergers and super massive black-hole binaries (Unwin et al. 2008), reverberation mapping (Shen 2012), extrasolar planets, etc. We do not need, now, to focus in an specific scientific target, but it is convenient to give an estimate of the astrometric accuracy that can be reached with GTC. According to Lindengreen (1978, 2005),
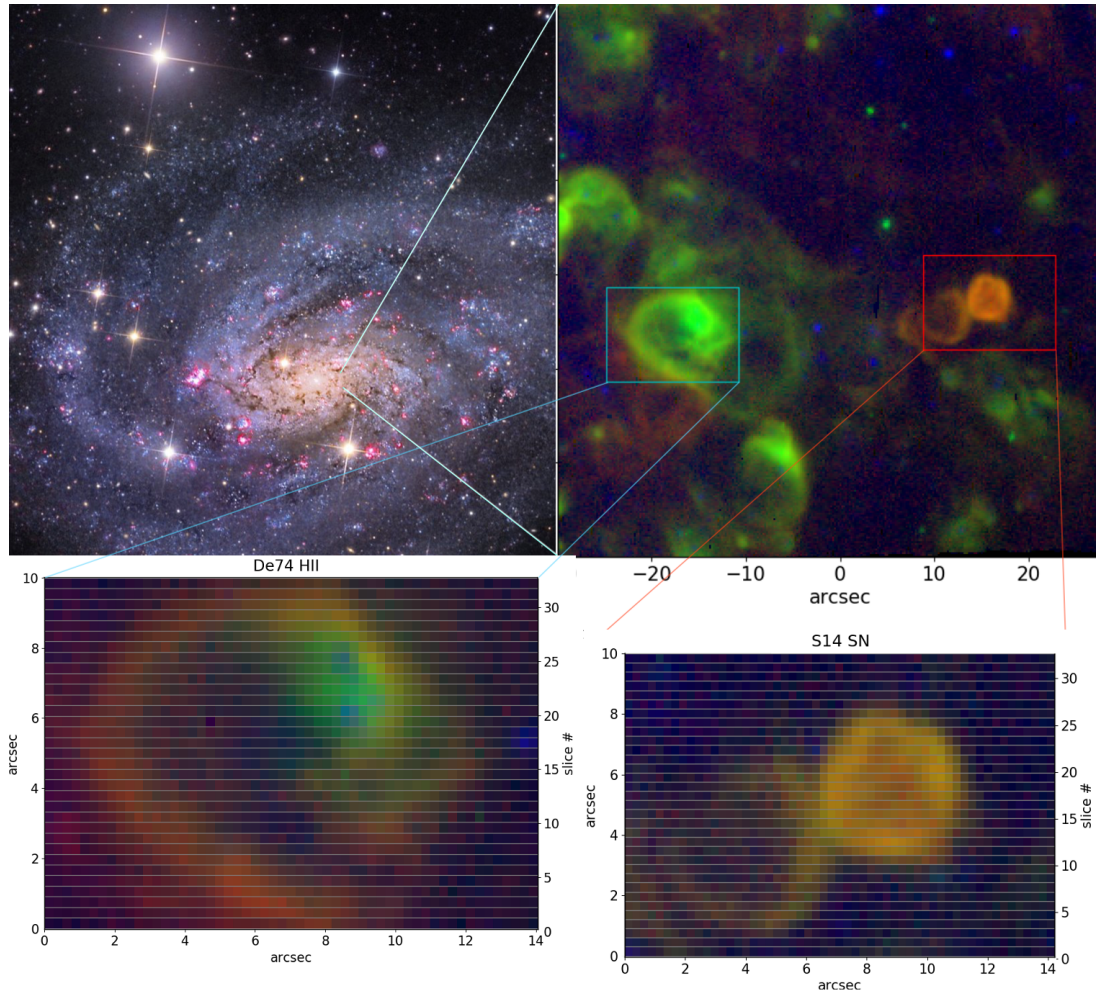
Figure 3. MAAT simulation of two nebular objects in the spiral galaxy NGC300. The HII region De74 (left) and the SN remnant S14 (right). The two bottom images is how the slicer sees each of the objects that are then dispersed onto the CCD to obtain the frames as in Figure 17.

assuming that the diameter of the telescope is 10.4 m and that we receive 10^5 photons from the source, we will have an astrometric accuracy in the determination of the photo-center at 6500 Å of 13 microarcsecs (not far from what is expected with the E-ELT at 1.6 micrometers).

All these advantages mentioned above among others are offered by MAAT@GTC, which it will provide to the GTC community with highly competitive unique observing capabilities, being complementary to the existing and upcoming instrumentation, i. e.,

1. Seeing-limited and wide-band IFS at low / moderate spectral resolution,

2. Advantage on bad (any) seeing conditions. MAAT keeps its nominal spectral resolution regardless the seeing conditions.

3. MAAT can perform spectro-photometry and spectro-astrometry,

4. Prompt to Targets of Opportunity - target acquisition with no overheads. An entire F.o.V. image could be generated from the 3D data cube,

5. All photons are collected, and hence one obtains a larger efficiency.

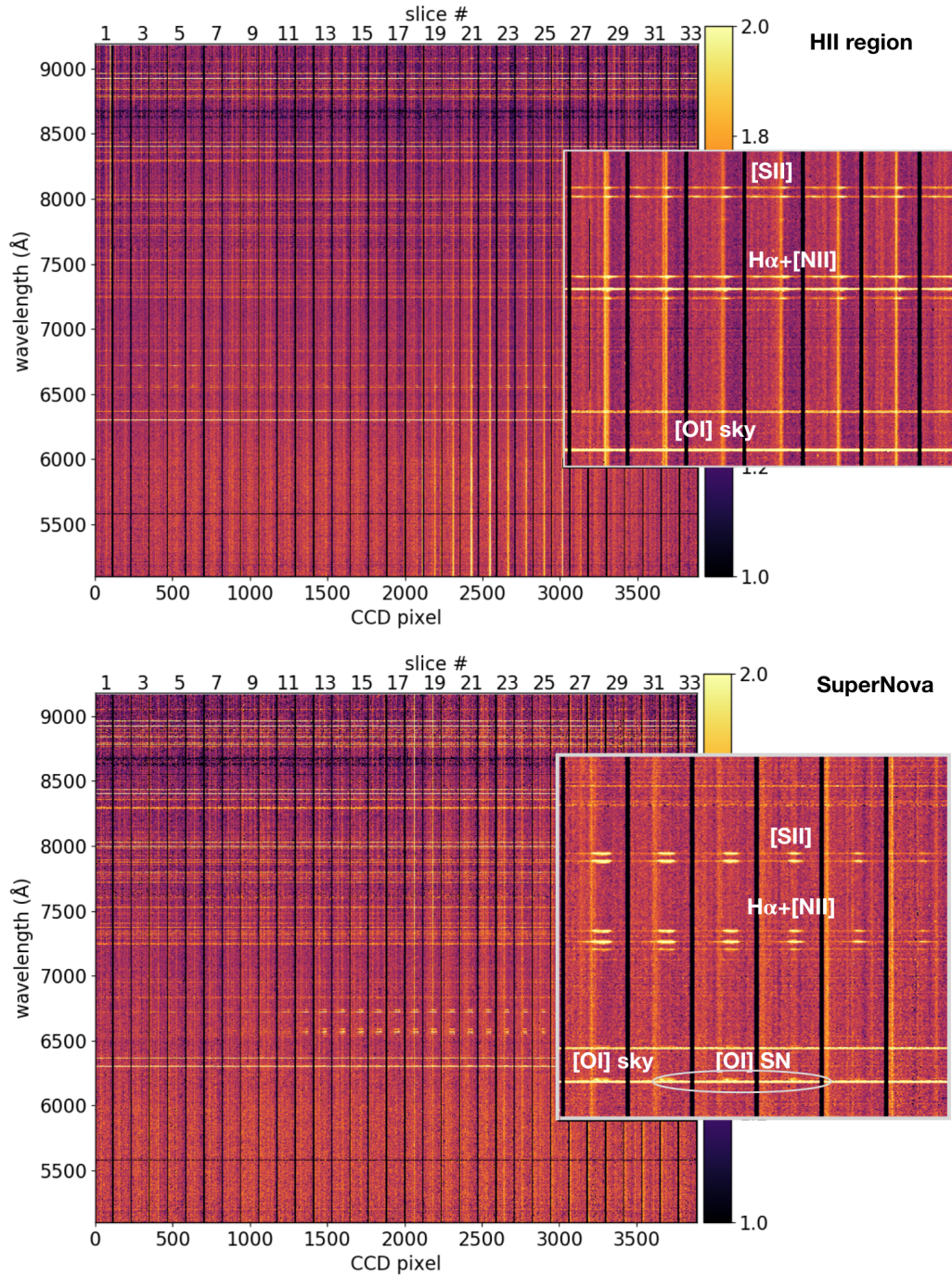6. MAAT will allow the GTC to reach its limit for deeper spectroscopy,

Figure 4. Top: MAAT simulation of the giant HII region De74 in the galaxy NGC300. The inset shows a zoom in around the [OI]6300 to [SII]6731 spectral region. Notice that the [OI]$\lambda\lambda$6300, 6364 are earth atmospheric emission lines, while the other emission lines in the inset are nebular lines in De74. Bottom: MAAT simulation of the SN remnant S14 in the galaxy NGC300. The inset shows a zoom in around the [OI]6300 to [SII]6731 spectral region. Notice that the strong [OI]$\lambda\lambda$6300, 6364 are earth atmospheric emission lines, while the other emission lines in the inset are nebular lines in S14. An ellipse around [OI]6300 marks how a faint [OI]6300 emission is detected in the SNR just redshifted with respect to the bright sky lines.

These unique capabilities are fundamental in order to develop the outstanding science objectives presented below. The scientific reach of MAAT@GTC is proving to be very substantial with a major impact on Astronomy and Cosmology.
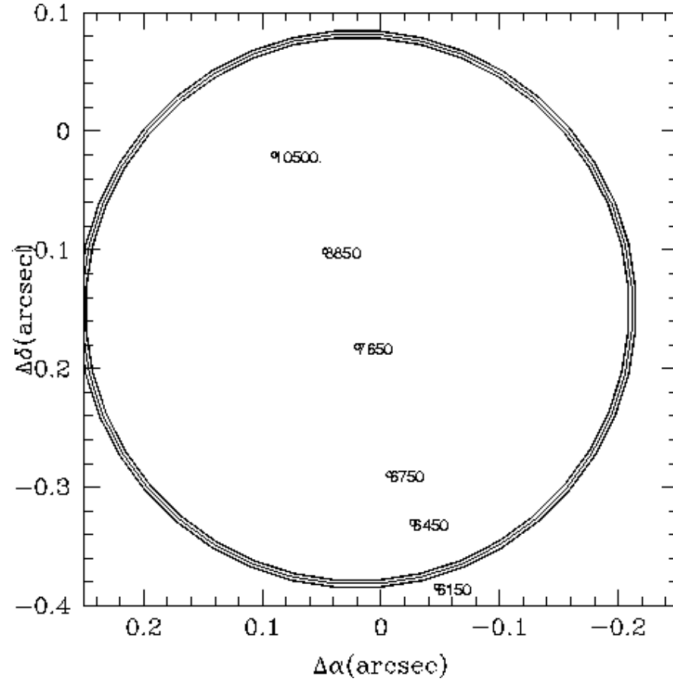
Figure 5. ....

3. SCIENCE OBJECTIVES

Our model of the universe has changed dramatically over the last two decades: we have come to realize that 95% of the cosmic composition is made of dark matter and dark energy and not in the form of baryonic matter that all of science had focused on for centuries. This drastic development was originated from novel astronomical observations facilitated mainly by technological advances. One of the key pieces in the paradigm shift in cosmology was the detection of the accelerated expansion of the universe (Riess et al. 1999; Perlmutter et al. 1999), attributed to an exotic component named "dark energy". This evidence was first observed through transient astrophysical phenomena, Type Ia supernovae (SN), used as distance indicators in cosmology (Phillips 1993a).

As we look forward, we can identify exciting new avenues where breakthroughs can be expected, many of them also involving astrophysical transients. To begin with, we have just witnessed the dawn of the era of multi-messenger astronomy. Mergers of binary compact objects, generating gravitational wave (GW) signals along with electromagnetic waves (and possibly neutrinos!), allow us to probe the densest states of matter and serve as laboratories for gravity at its most extreme conditions. At optical wavelengths, the resulting phenomena, dubbed *kilonovae*, hold great promise for scientific explorations ranging from the origin of heavy elements through r-process reactions (Smartt et al. 2017; Watson et al. 2019), to the most accurate studies of the expansion of the universe (Abbott et al. 2017a; Hjorth et al. 2017; Dhawan et al. 2019).

Gravitational lensing offers yet another way to study the power of gravity and the properties of curved space-time, thereby tracing the nature and distribution of dark matter and dark energy in an independent way. Gravitational lensing of transients, most notably quasars and supernovae, is emerging as a new precision tool in astronomy: in addition to the spatial information, these time-structured light beacons allow us to measure time-delays between light rays deflected by bodies in the line-of-sight (Refsdal 1964). These deflectors come in many different shapes and mass-scales: black holes, stars, galaxies, and galaxy clusters. Gravitational lensing offers unique ways to weigh these structures, along with the measurement of global cosmological parameters, most notably the Hubble constant H_0 (Treu 2010).
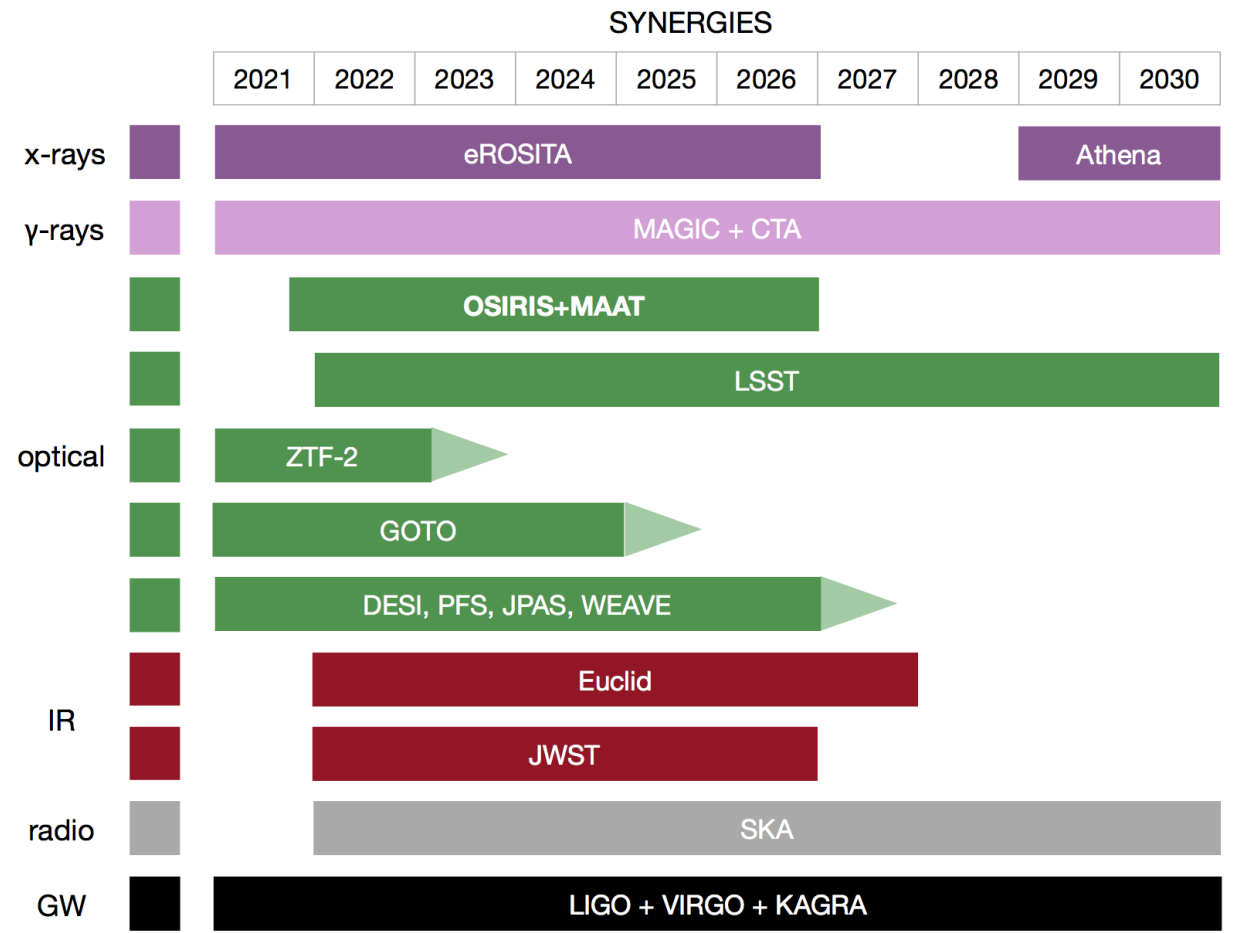
Figure 6. Synergy chart of OSIRIS+MAAT in the timeline context of upcoming major facilities. MAGIC, CTA, WEAVE, and GOTO are located at the ORM.

These intrinsically very rare phenomena can now be detected by large scale imaging surveys operating at optical wavelengths scanning the heavens with unprecedented speed and efficiency. Projects like ZTF[3], PanStarrs[4], ATLAS[5], GOTO[6], and soon LSST[7], uncover the variable sky in ways that have not been possible until now. It is in this context, that the proposed instrument becomes the critical missing element. While imaging surveys are essential for the discovery of rare transients, timely identification of the nature and evolution of transients and their host galaxy environments requires spectroscopic screening in a telescope with great light collection power. Thus, the proposed IFU for OSIRIS on the 10-meter Gran Telescopio de Canarias, MAAT, presents us with unique opportunities to complete the time-domain revolution in astronomy.

Add here a couple of paragraphs that set the scenes for other research topics included in the white paper, in particular galaxy formation, brown dwarfs and planetary mass objects and nebulae ... something general that will balance the above text on time-domain astronomy.

The GTC equipped with OSIRIS+MAAT will play a fundamental role in synergy with other facilities operating in La Palma, opening a new era for transient studies at the Observatory of the Roque de Los Muchachos (see Figure 6). Furthermore, the MAAT top-level requirements allow to broaden its use to the needs of the GTC community for a wide range of competitive science topics given its unique observing capabilities well beyond time-domain astronomy.

---

[3] https://www.ztf.caltech.edu

[4] https://www.ifa.hawaii.edu/research/Pan-STARRS.shtml

[5] https://fallingstar.com/home.php

[6] https://goto-observatory.org

[7] https://www.lsst.org

While the science potential of MAAT@GTC is essentially unlimited, this white paper will highlight the focus on a selected set of outstanding science topics enabled by the proposed instrument in different areas of expertise. These include,

- Characterisation of the diffuse universe: the intergalactic and circumgalactic mediums

- Strong galaxy lensing studies,

- Black holes in QSOs and stellar remnants,

- Time-delay measurements of strongly lensed supernovae and quasars,

- Identification and characterisation of EM-GW counterparts,

- Exploration of the host galaxy environment of Type Ia SN, Kilonova and other remnants,

- Brown dwarfs and planetary mass objects,

- Synergies with the JWST, Euclid, and other facilities,

- Potential discovery and characterisation of the transient sky,

- Binary masses and nebulae studies;

described in the sections below.

3.1. *Characterizing the CGM and IGM of galaxies with MAAT: two practical cases at two extreme redshifts*

Numerical simulations predict that gas accretion from the cosmic web drives star formation in disk galaxies (e.g., Sánchez Almeida et al. 2014). The process is particularly important in the early universe, but it also occurs in isolated dwarfs of the local universe. The cosmic gas is expected to coexist with gas from galaxy-wide winds driven by feedback from star-formation and AGNs. Although this cosmic gas accretion is a central ingredient of the current theory of galaxy formation, it has not been observationally confirmed yet, and MAAT@GTC may play a fundamental role in this confirmation. MAAT FOV ($14.2" \times 10"$) is insufficient to carry out blind searches for diffuse gas in the CGM and IGM of galaxies (Circum-Galactic Medium and Inter-Galactic Medium), however, its FOV, spectral coverage, and spectral resolution allow chemo-dynamical studies to distinguish metal-poor inflows from metal-rich outflows. Examples of two studies at extreme redshifts are: **(Case 1)** is the HI plume of IZw18 pristine gas in process of being accreted (Fig. 7, top; Lelli et al. 2012)? **(Case 2)** What is happening in and around the $z \sim 3$ enormous Lyα nebula SDSSJ1020+1040 (Fig. 7, bottom; Arrigoni Battaia et al. 2018)?. The shape of the Lyα line allows to distinguish between inflows and outflows.

3.2. *Improving strong lensing models with MAAT*

Strong gravitational lensing (SGL) allows to directly map the distribution of mass in massive clusters, where background galaxies can be observed as multiple images. Each one of these images carries information about changes in the potential along the line of sight. In most cases, most of this change in the potential takes place in a relatively small volume around the lens. Detailed maps of the lensing potential can reveal substructures in the dark matter, that can later be linked with models of dark matter, such as the standard cold dark matter scenario, or more alternative models such as self-interacting dark matter, axion-like particle dark matter, or even primordial black holes. To reach this level of detail, robust confirmation of the lensed systems, accurate measurements of the redshifts of the background galaxies, member identification of galaxies in the cluster, and if possible, independent mass estimates of the mass based on velocity dispersion, are needed. IFS has proven extremely valuable in the last years in confirming lensed systems in crowded fields, such as massive galaxy clusters. The Hubble Frontier Fields program (HFF) is the state of the art in galaxy cluster lensing. As part of the HFF program, six clusters were observed to unprecedented detail. These observations unveiled hundreds of background lensed galaxies. Spectroscopic confirmation of most of the lensed galaxies and their counterimages in these clusters has been possible mostly thanks to instruments equipped with IFS capabilities (such as MUSE). IFS is been used also to identify features, or knots, in giant arcs that are multiply lensed, as shown in Fig. 8. Very often, matching pairs of images that are multiply lensed within the same giant arc is not
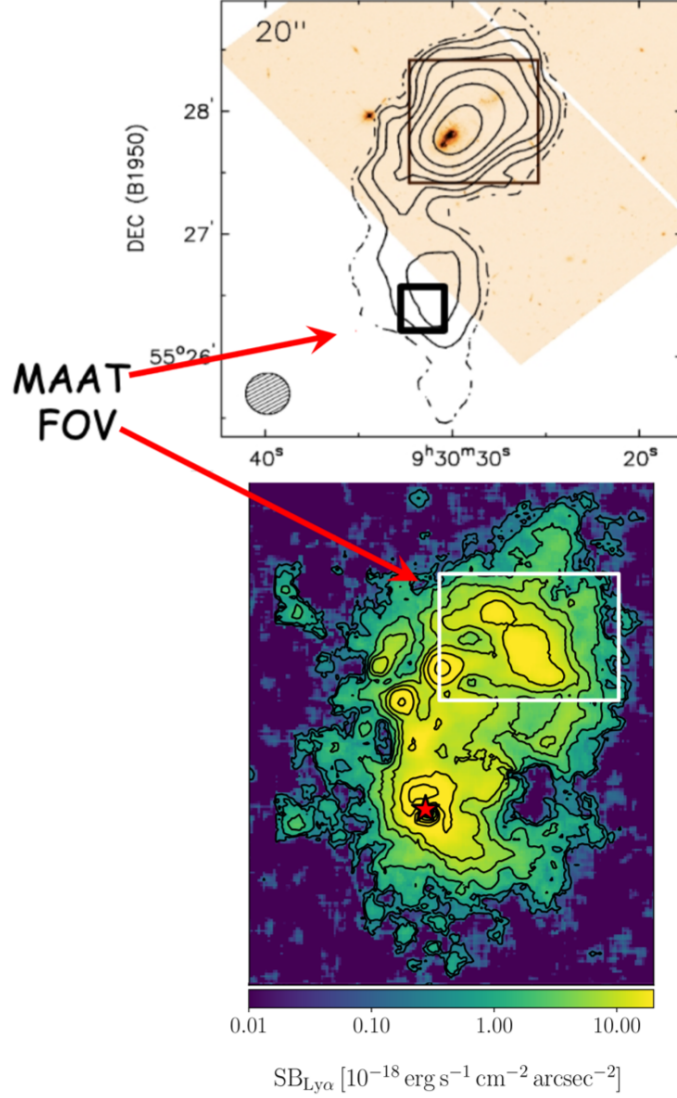
Figure 7. *Top:* HI emission around IZw18 (the contours, from Lelli et al. 2012). MAAT@GTC will allow us to discover whether the observed HI plume is pristine gas in process of being accreted onto the galaxy (the background image). *Bottom:* Lyα emission around the $z \sim 3$ radio-quiet quasar SDSSJ1020+1040 (red star) (figure adapted from Arrigoni Battaia et al. 2018). MAAT@GTC will allow us to distinguish between inflows and outflows.

trivial given the rich substructure commonly present in these arcs. IFS can provide the fingerprint signature of each one of these signatures, facilitating their matching. The identification of these knots is of great interest to pin point the position of the critical curves, or to compute flux ratios, which can later be used to improve on the lensing models, or to identify substructures down to scales as small as thousands of solar masses. Also, IFS can be used to estimate the mass of individual member galaxies in the cluster. This is particularly important for the central BCG, since lensing constraints are typically scarce near the BCG, and velocity dispersion measurements from IFS data can provide a much needed anchor point for the central mass in the lens model.

IFS observations are also useful to identify regions in the lensed galaxies near the critical curves with very active star formation rates. These active regions are expected to harbor very bright, but short lived, stars, that can be observed after being magnified by factors of hundreds to thousands. These regions are ideal targets to search for transients produced by bright stars crossing the caustic of the cluster, or more likely microcaustics produced by intervening microlenses in the cluster. These microlenses can be stars in the intracluster medium, but also dark matter cabdidates like primordial black holes, or small scale fluctuations in the dark matter distribution (that corrugate the critical curves)
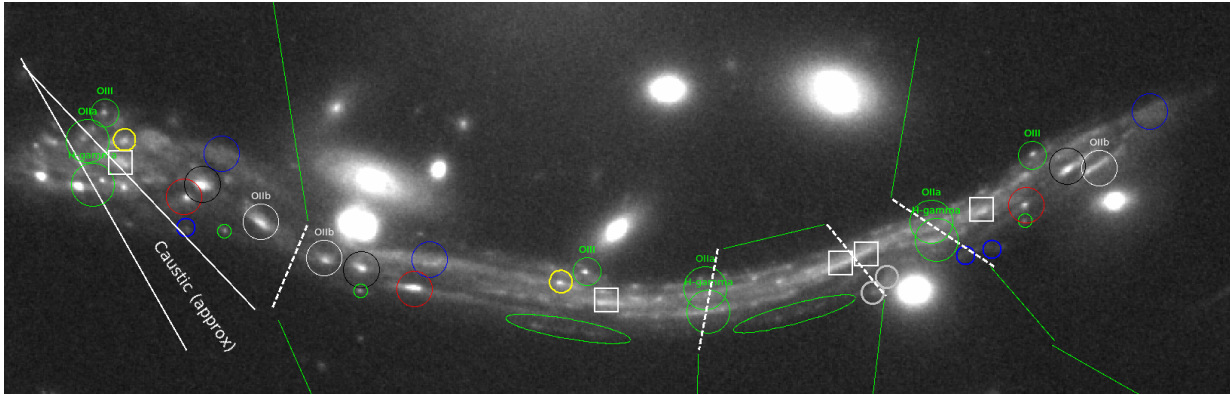
Figure 8. Giant strongly lensed arc in the galaxy cluster A370 as seen by HST. The arc corresponds to a foreground galaxy that is being multiply lensed 5 times. Identification of multiply lensed features is possible with IFS data from MUSE, that can resolve individual compact regions in the foreground galaxy through their emission lines. The feature identification form IFS data can be used to build a model independent model of the critical curves (dashed lines), that can later be confronted with actual lensing models.

produced by interference in wave dark matter models. Such observations are already a reality after the discovery of the first such event (Kelly et al. 2018; Diego et al. 2018).

3.3. *Identification and characterization of EM-GW counterparts*

The detection of gravitational radiation from the binary neutron star (BNS) merger, GW170817 (Abbott et al. 2017b), along with a short gamma-ray burst (sGRB) just 1.7 seconds later (Goldstein et al. 2017), followed by the identification of an associated kilonova AT2017gfo in the nearby galaxy NGC 4993, at just 40 Mpc distance (Arcavi et al. 2017), opened a new multi-messenger window in astrophysics and cosmology. The forthcoming observational runs by the enhanced-sensitivity interferometers Advanced LIGO/VIRGO and KAGRA will extend the reach of possible additional kilonova detections to about 200 Mpc distance. These events will become the targets of the most intense observational campaigns in time-domain astronomy. Our knowledge about kilonova physics currently relies on the sole detection of GW170817/AT2017gfo (Abbott et al. 2017b), which has raised a number of very important questions about the connection of BNS mergers and short GRBs, the production of heavy elements in the Universe, as well as the potential use of BNS-mergers as "standard sirens" for cosmology. Furthermore, important open questions remain about the history of the stellar populations leading to the BNS system progenitors. MAAT@GTC will shed light on the formation and evolution of compact objects, emission processes and the expansion rate of the universe by addressing a set of these open questions through an accurate analysis of high-resolution and IFS data of the kilonovae and their host galaxies. Using a set of apposite techniques, developed to study the stellar population, structure and dynamics of gamma-ray bursts and superluminous supernovae host galaxies through IFS, we can study, with an unprecedented accuracy, the properties of the kilonova progenitors parent stellar populations, such as the star formation history, metallicities in the immediate circum-burst environments, and make use of the dynamical information to determine the evolutionary history of the neutron star binary system, as well as to determine the host galaxy distance and sharpen the measurement of the local expansion rate of Universe, the Hubble constant H_0.

This information can be obtained with the use of new powerful synthesis population codes for the analysis of single and binary stars (with or without stellar rotation implemented, Cid Fernandes et al. 2013; Eldridge et al. 2017). The use of advanced methods coming from machine learning techniques, aimed to find the best stellar templates, will also provide the nebular component of the immediate environment, obtained with a simple subtraction of the best stellar template, and consequently allow the information of the gas component around the kilonova source (see as an example Figure 9, which refers to the so far unique case of KN 170817A, Levan et al. 2017).

The IFS observations that will be carried out with MAAT@GTC will also allow to follow-up the electromagnetic counterparts of newly-detected gravitational signal events and will help in building multi-epoch spectral energy distributions. Among the many advantages provided by MAAT with respect to other similar operating IFUs in 10m-class telescopes, like MUSE at VLT/ESO, the coverage of the "blue" region of the optical spectrum represents one of the most important additions. The early emission from kilonovae , belived to originate from radioactive decay of unstable r-process elements, is characterised by a very hot black body spectrum, with the peak of the thermal emission in
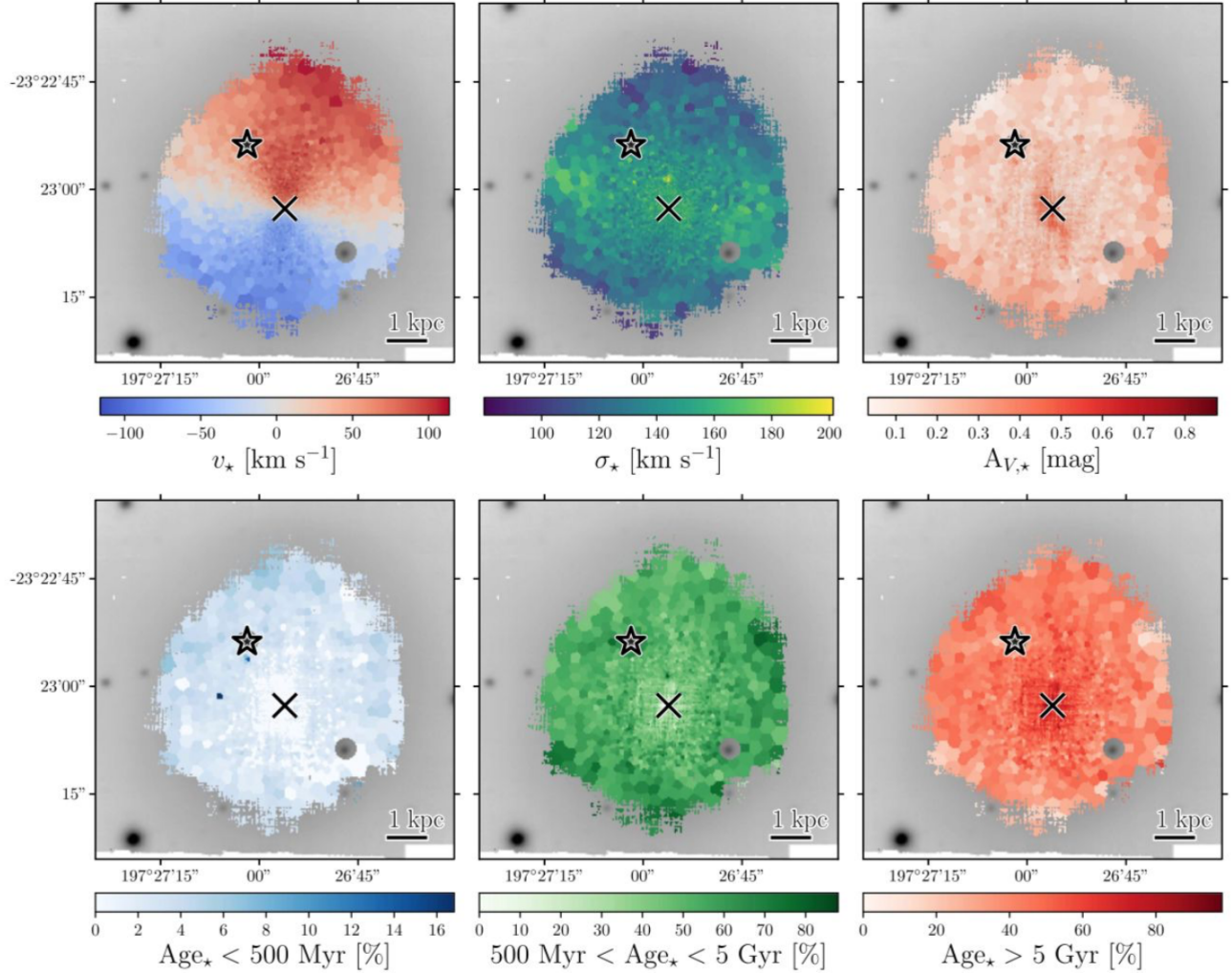
Figure 9. Stellar population map for NGC 4993 obtained with MUSE (Levan et al. 2017). The upper panels show the distribution of the radial velocities (left) as estimated form the stellar components for each single spectral bin, as well as its dispersion in terms of σ (middle) and the extinction as inferred from the fit continuum (right). Lower panels show the distribution of stellar ages for different age intervals: less than 500 Myr (left), between 500 Myr and 5 Gyr (middle) and larger than 5 Gyr (right). The black star corresponds to the location of the kilonova AT2017gfo.

the earliest instances is located at near-UV/blue wavelengths. In the days that follow, the emission originates from a lanthanide rich region, the kilonova ejecta cools down implying a redder thermal emission peaking in the near-IR. Consequently, the early peak of the kilonova emission, containing information of the viewing angle and geometry of element composition, is more intense at blue wavelengths, where MAAT is particularly sensitive. In Figure 10 we show an example drawn from the X-shooter spectral series of the kilonova AT2017gfo (Pian et al. 2017), which shows the potential of investigating the blue region of the wavelength spectrum as provided by MAAT: several transitions of r-process elements fall in this spectral region (we mention the possible resonance line of Sr II 4077-4215 Å), which points out to an important role for MAAT@GTC for kilonova science in the years to come.

The observational strategy strongly depends on the number of detections of strong candidates by the LIGO-VIRGO Collaboration. The expected start of MAAT observations will coincide with the next observing run (namely the O4 run, expected to start observations in late 2021) at the LIGO-Virgo inteferometers, which will be characterised by an improved detector sensitivity and then a larger distance threshold for BNS detections. At the same time, the LSST will start to observe the full-sky visible from Chile, providing potential candidates for each GW detection at very deep magnitudes (current estimates give limits of r $\sim$ 24.5 mag for a single exposure with LSST). Similarly, optical surveys in the Northern hemisphere will scan the error region of each GW detection (we mention the GOTO telescope,
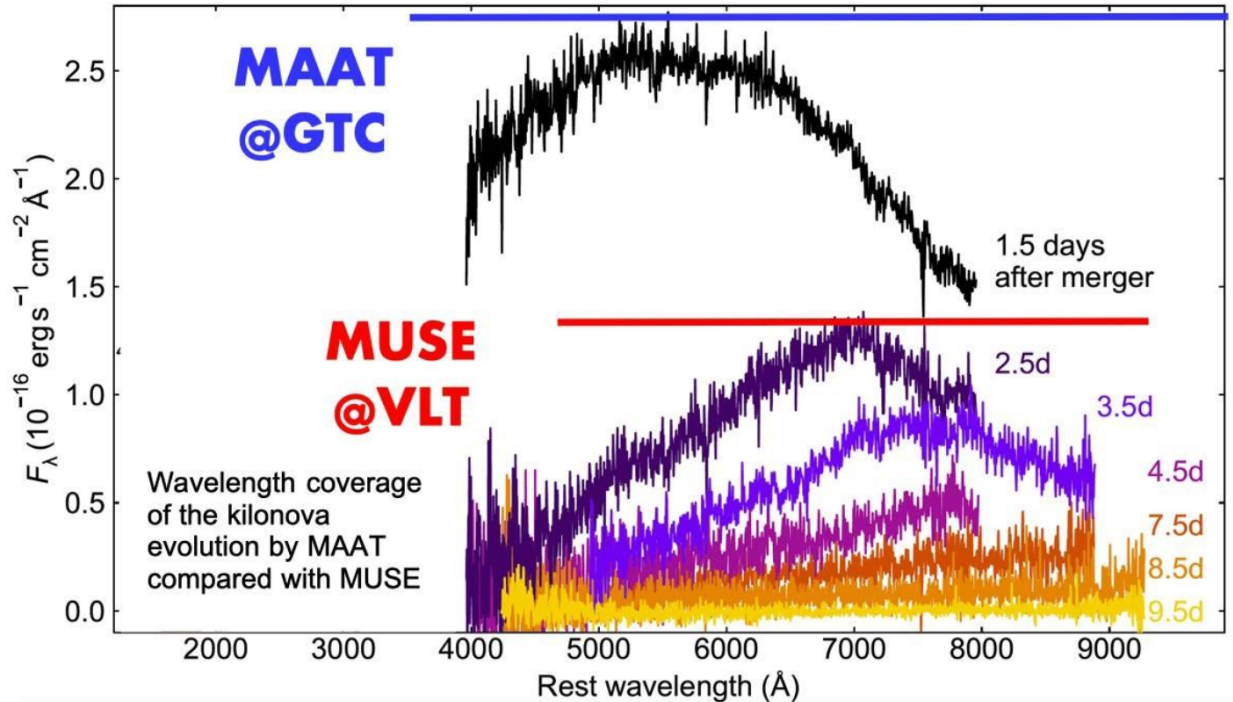
Figure 10. The spectral time series of kilonova AT2017gfo during the first 10 days of its emission (Pian et al. 2017). We highlight the broader wavelength coverage that can be observed with OSIRIS+MAAT (blue line), using a combination of the R1000B and R1000R grisms, as compared to MUSE (red line).

currently operating in La Palma whose synergy with MAAT@GTC is fundamental for the success of the program) providing then possible candidates for each BNS merger detected by LIGO-Virgo. According to the detection rate for binary neutron stars (BNS) during the current O3 run (five BNS detections in eight months of observations) and considering that GTC will cover $\sim 60\%$ of the entire sky (excluding southern latitudes and Sun-constrained regions of the sky) we expect to observe two BNS candidates per semester.

According to the above considerations, the strategy that we intend to adopt in a single semester of observations, will consist in obtaining a first observation in Target-of-Opportunity mode as quickly as possible once the error region is down to the size of the MAAT field of view - providing immediate information about the transient. Given the rapid evolution of kilonovae (they fade very quickly after two weeks from the BNS merger) we will ask for additional epochs very close in time: we plan three or four more epochs to be distributed in the first 10 days of the KN emission. A late observation, to be executed once the source has faded, then at any time, is necessary in order to provide direct information about the stellar population underlying the source position. Each single BNS event will then require a set of 1 hour, which corresponds to a total requested time of 20 hours.

The kilonova AT2017gfo at the distance of 40 Mpc represents our best reference event to be used in our analysis to quantify the number of expected events within the reach of MAAT. According to the observed evolution and the distance of 40 Mpc of AT2017gfo, and given the sensitivity of MAAT, we expect to observe the peak brightness emission of kilonovae at the distance of 200 Mpc (expected magnitude V$\sim$19.5 mag) with a signal-to-noise of $\sim$10 per spectral bin assuming standard 1$\times$1 binning and the use of the R1000B grism. This estimate will improve if we integrate over the entire PSF of the source, permitting us to follow the evolution of the KN with similar signal-to-noise values below 2-3 magnitudes from the peak, which is equivalent to cover a week in terms of kilonova evolution (see Figure 10).

Kilonovae are also promising accurate distance indicators. As demonstrated by Dhawan et al. (2019), the H_0 estimate using the "standard siren" measurement of GW170817 could be significantly improved by using the wavelength dependent intensity of the EM counterpart, AT2017gfo. The reason for this is that the time dependent SED of the kilonova is sensitive to the viewing angle towards the BNS merger plane. Since the latter is degenerate with the distance estimate from the GW signal, MAAT@GTC would allow us to do the same "standardization" for BNS merger GW distance out to 200 Mpc, i.e., the volume probed by the interferometers, and beyond the distance to which

one can safely expect viewing angle constraints from radio data when a GRB is observed (about 10% of the cases). Furthermore, the latter requires high-density interstellar medium surrounding the GRB, unlikely to be the case for many of the BNS mergers. In summary, kilonovae observations with MAAT offer unique possibilities in this thriving field.

3.4. *Time-delay measurements of strongly lensed supernovae and quasars*
3.4.1. *Strong gravitational lensed quasars*

The time-delay distance inferred from strong gravitational lensed quasars can be used as a powerful estimator of the Hubble constant and the main cosmological parameters. Quasars are very luminous astrophysical sources, so they can be observed from large distances. This makes them not only fascinating objects of study, but also useful as markers for studying Hubble-Lemaître's Law. Indeed, light emitted from quasars fluctuates; when the follow-up of this variable luminosity is observed through multiple lensed images in gravitational lensed systems it can provide a direct measurement of distance (Refsdal 1964), which is independent of local calibrators generally used in the cosmological distance scale ladder. This method is based on the measurement of the time-delay between two or more images, and on the a priory knowledge of the intervening lens mass, and it is so powerful that just three lenses are needed to determine H_0 with a precision of 3.8% (Bonvin et al. 2017; Shajib et al. 2019). Increasing the number of lensed quasars, for which we can infer the value of the Hubble-Lemaitre constant H0, will then improve the accuracy on H0 and this indicates the kind of contribution that MAAT will provide to fundamental cosmology in mediating the current tension between the Planck and local distance ladder estimates of H0.

IFS observations of lensed quasars can spatially resolve the kinematics of the deflector lens, enabling a large improvement in breaking the mass-anisotropy degeneracy and leading to a more accurate mass model for the lens, which will lead to a considerable improvement on the H_0 value (Shajib et al. 2018; Birrer et al. 2018). The primary distance measurement is given by the time-delay distance, which is a multiplicative factor that depends on three angular diameter distances, the distance to the observer, the lens, and their relative distance. The combination of these measurements with the spatial and spectral information coming from the deflector lens (its stellar velocity dispersion, a proxy for the lens potential) will provide the angular diameter distance to the lens in a unique and independent way, which can then be used to constrain the cosmological parameters in the context of the standard (and non standard) cosmological models (Grillo et al. 2008; Paraficz & Hjorth 2009; Jee et al. 2015).

In the Sloan Digital Sky Survey (SDSS) the number of lenses found is larger than expected from the most optimistic theoretical predictions (Oguri et al. 2005). The total number of lensed quasars depends on the limiting magnitude of the observations: assuming a value of $r = 20$ mag, we have a total number of ~ 200 sources visible from La Palma. However, we need a statistically significant number (e.g. 40-50) of quasars in order to get a very good precision on the Hubble-Lemaitre constant and then make important constraints on the cosmological parameters and models. We will focus on the quasars that will fill the MAAT field of view and that are enough bright to follow-up in time the variable light emitted by the lensed quasars: as an example, the quasar SDSS 1206+4332 (Birrer et al. (2019), see Figure 11) extends over a region that can be completely covered by MAAT in a single shot. Multiple dithered exposures will deliver a better resolved and high spectral quality dataset that, combined with the MAAT spectral and spatial resolution, can provide an exquisite measurement for the spatial kinematic distribution and the velocity dispersion of the lens potential, while observations in time will give an estimate for the quasar emission time-delay. Taking the SDSS1206+4332 source as model, characterised by g=17.6 mag and i=17.4 mag, a single exposure of 300s, using the R1000R grism, will provide a S/N value of 30 for the quasar spectral emission. Although for the time-delay measurements we can also use much shorter time exposures, longer exposures are preferred in order to enhance the faint signal from the lens sources and the fainter background galaxies that can belong to the cluster, in the case of a cluster lens.

We will focus on ~ 10 quasars per semester. This will imply a total observing time of 10 hours per quasar, and then a total requested time of 100 hours per semester at the GTC. This type of analysis has recently been applied using data from MUSE at VLT (Caminha et al. 2017, 2019; Bergamini et al. 2019). The lack of an instrument like MUSE at northern latitudes, with the only exception of KWCI at Keck (which only covers the blue spectral range), will render MAAT a very competitive instrument for this type of science.

3.4.2. *Strong lensed supernovae*

The recent discoveries of strongly lensed supernovae (Kelly et al. 2015; Goobar et al. 2017) have opened yet a new road to study the high-redshift universe as well as the physics of supernovae at large distances, when the Universe
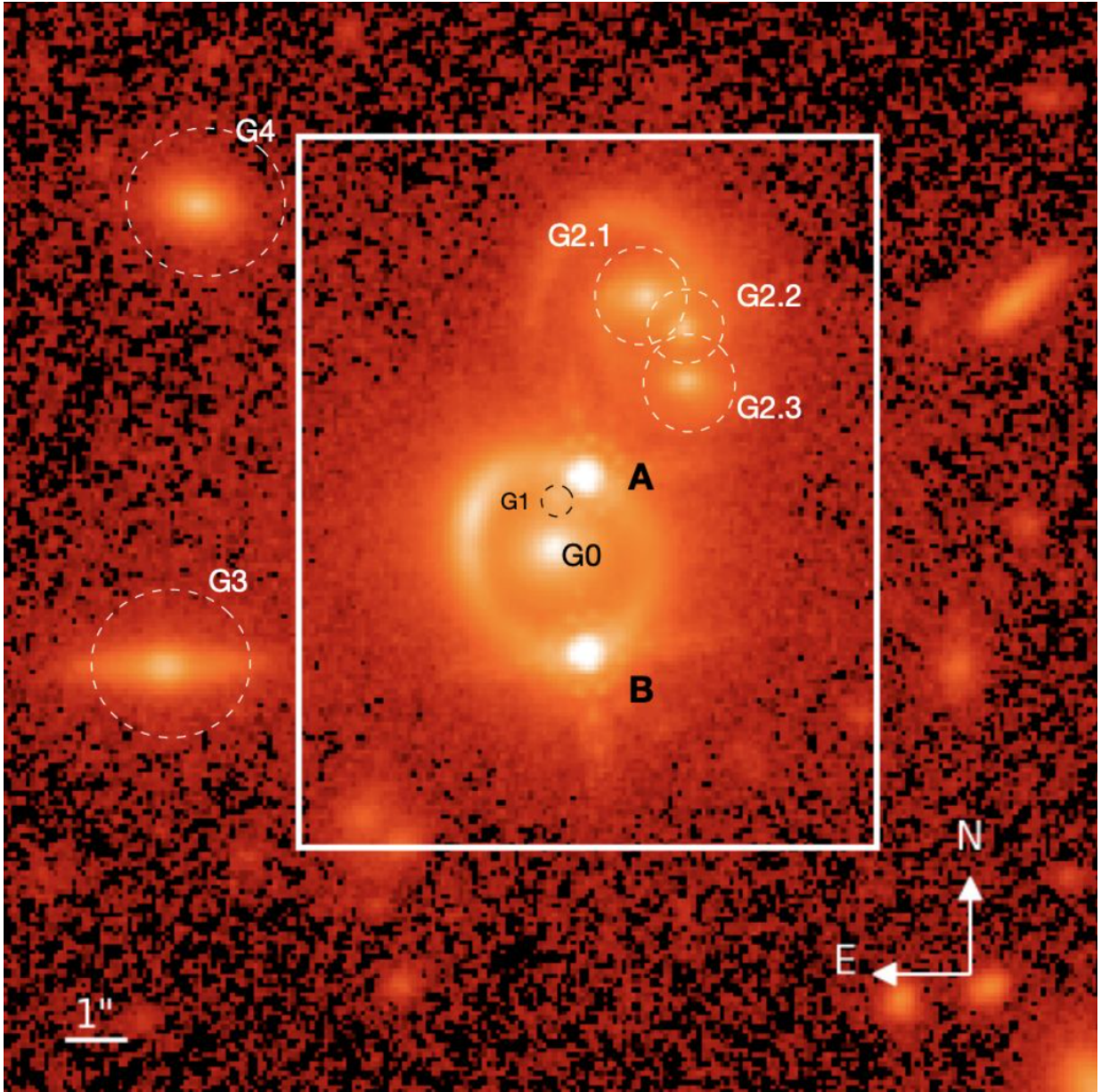
Figure 11. The lensed quasar SDSS J1206+4332. The lensing galaxy G0 is located in the center of the image. A and B are the double quasar lensed sources. G2 is a triplet galaxy, and G3 and G4 are other nearby galaxies. The white rectangle marks the field of view of MAAT. Image Credit: Hubble Space Telescope (Birrer et al. 2019).

was much younger. In particular, with lensed SNe Ia, it is possible to combine them as standard candles through the well-known light curve correlations (Phillips 1993a; Perlmutter et al. 1995) and at the same time via the lensing time-delay between multiple images, which was recently used to determine the Hubble constant (Grillo et al. 2018). Projects like ZTF and in the near future LSST will find large numbers of lensed SNe (their simulations predict a number of 10 lensed SNe in three years of operation, Goldstein et al. 2019), at which point follow-up facilities will be in very high demand. The current Young Supernova Experiment survey (Jones et al. 2019), using the PanSTARRS telescopes to catch the light of SNe at the very early stages of their explosion, is expected to observe four lensed SNe in 2 years, with the exact rate depending on the time cadence of each field of view and the lensed sources inside them covered by the survey.

The spectral capabilities provided by MAAT will allow us to study the SN light-curves, as well as the host galaxy environments and lensing galaxies of these lensed SNe at high redshifts, given the large signal-to-noise provided by the

large magnifications. Unlike strongly lensed quasars that require multiple and continuous monitoring in time, supernova time-delays can be measured in just weeks, as shown in Dhawan et al. (2019). Furthermore, as the supernovae fade on time-scales of months, these systems lend to unique measurements of the lens system and SN host galaxy which are unfeasible for quasars (Mörtsell et al. 2019) and allow for exciting measurements of substructures through microlensing effects (Goobar et al. 2017; Dhawan et al. 2019; Mörtsell et al. 2019). Intriguingly, Johansson et al. (2020) showed that spectroscopic measurements alone can provide competitive measurements of time-delays for SNe Ia, an exciting new avenue that can be exploited with MAAT.

The spatial and spectral information on the lens and the time-delay signal as provided by MAAT, in a single shot repeated in a fixed number of exposures - the already mentioned 4D spectroscopy –, will permit to constrain the Hubble constant through the measurement of time-delay effects, as described for quasars, and at the same time infer the distance through the use of luminosity relationships, as successfully applied in recent years to SNe Ia, which have lead to the discovery of the acceleration of the Universe (Riess et al. 1999; Perlmutter et al. 1999). Finally, MAAT observations will also probe evolutionary effects of supernovae and their environments through spectroscopic observations of highly magnified high-redshift cases, unveiling the luminosity function distribution up to high redshifts.

The expected rate of newly-discovered strong lensed supernovae is relatively low: from ZTF Goldstein et al. (2019) expect ~ 5 lensed supernovae (of all types); while the expectations from LSST are more optimistic: ~ 170 lensed supernovae in one year. The observations requested for this program are of the type Target-of-Opportunity, given that we do not know in advance when and where a lensed SN will be discovered. Moreover, we need additional observations in order to monitor the appearance of multiple deflected emission by the lens source. Consequently, we will focus, initially, on a limited number of targets (2-3) per semester, asking for a total number of 5-6 epochs per SN.

The observation itself of lensed SNe, in particular SN Ia at redshift $z = 1.0$ is not an easy task. However, the lensing brightness amplification will improve the detectability for high-z SNe, which represents a unique occasion to study the far Universe with these sources. Assuming a spatial binning of 2×2 and R300R grism, for one hour exposure time (4×900s) we expect to observe with MAAT a SN of $V = 23.0$ mag with a $S/N \sim 10$, for the region around 4000-4500 Å where SN features of Fe II, Ca II and Mg II are generally observed. Following epochs will require longer exposures, unless we further bin the spectrum, which however will make us lose only a limited information on the spectral emission. Again, this program cannot be performed with MUSE at the VLT due to his blind sensitivity below 4800 Å.

3.5. *Cosmology and Fundamental Physics with Gravitationally Lensed Quasars*

Time-delay cosmography was proposed by Sjur Refsdal in 1964 and is now proving to be a competitive probe of the expansion history of the Universe. In gravitational lensing, the light from distant sources is deflected by the gravity of intervening massive objects, and even split into multiple images when the source and the deflector are closely aligned. When the source is variable, the slightly different path length across multiple images results in measurable time-delays (typically spanning 20d-120d), which in turn are directly related to the distances to the deflectors and the sources. The H0LiCOW and then the TDCOSMO collaborations (Suyu et al. 2017, Millon et al. 2020) have shown that this effect can lead to few-percent uncertainties in the Hubble constant H0, in a way that is completely independent from any distance-ladder anchoring (e.g. Cepheids or TRGB), and even allow a first peek into possible new physics beyond the concordance paradigm (Arendse et al. 2020). However, to turn the measured time-delays into distances and H0, accurate lens models are required. These, in turn, require 10% accurate velocity dispersions of the deflectors and redshifts and stellar masses of other galaxies along the line of sight, to break the so-called "mass sheet degeneracies" (Falco et al. 1985; Sluse Schneider 2013) that would otherwise bias H0 significantly. Therefore, highly-multiplexed spectroscopy is key to accurate measurements. For lenses visible from the South, VLT-MUSE has been pivotal in reaching this aim: Shajib et al. (2020) have reached H0 to within 4% from just one lens, and the combination of six lenses (of which three with MUSE data) has yielded H0 within 2.4%. In the foreseen sample of 12 lenses discovered by STRIDES and followed up by TDCOSMO, H0 can be brought to 2% uncertainties with ancillary data of sufficient quality. Further into the ELT era, 40 lenses with measured stellar kinematics can bring H0 to within 1% and build a distance ladder that is entirely based on time-delay lensing distances (Jee et al. 2015, Shajib et al. 2018) over the 0.3<z<2.5 redshift range, i.e. the same as current and upcoming BAO endeavours. However, half of the lenses are in the North, and not accessible to MUSE or any other publicly available spectrograph with the same multiplexing capabilities. Tens of new time-delay lenses have been discovered over the last decade, including lenses in the North that the COSMOGRAIL and TDCOSMO teams are following up for time-delays and high-resolution imaging models.
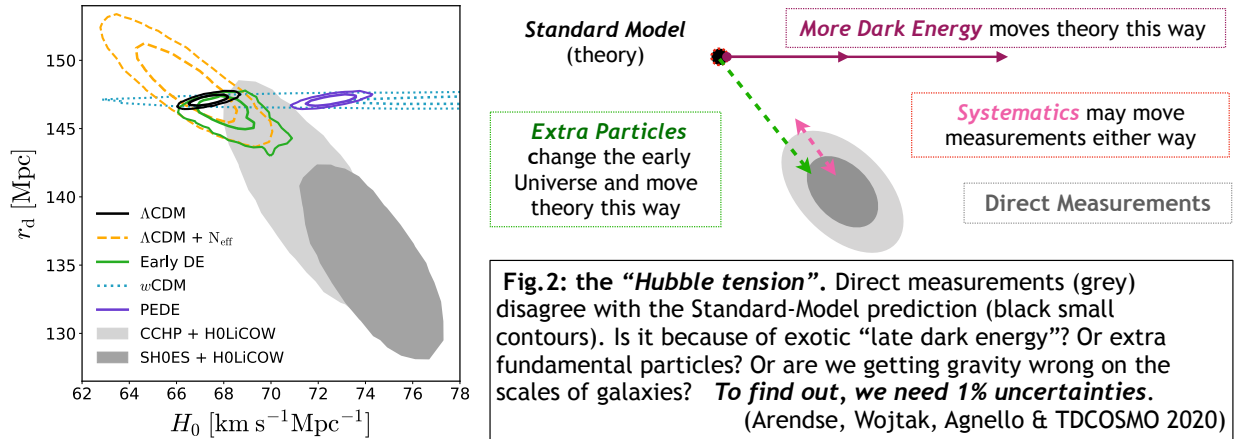
Fig.2: the *"Hubble tension"*. Direct measurements (grey) disagree with the Standard-Model prediction (black small contours). Is it because of exotic "late dark energy"? Or extra fundamental particles? Or are we getting gravity wrong on the scales of galaxies? *To find out, we need 1% uncertainties*. (Arendse, Wojtak, Agnello & TDCOSMO 2020)

Figure 12. The ....

As a spin-off, MAAT can also provide a super-resolved study of distant quasars and their host galaxies, using the same gravitational lens systems. As a matter of fact, there are even some known "coronagraph lenses", where the narrow-line region around the central engine of the source is stretched over wide arcs and even mapped in a different location from the broad-line region (e.g. Koopmans Treu 2002, Agnello et al. 2016).

3.6. *The environment of intermediate-z supernovae*

Type Ia supernovae (SNe Ia) are the most mature and well-exploited probe of the accelerating universe, and their use as standardisable candles provides an immediate route to measure dark energy. This ability rests on empirical relations between SN Ia peak brightness and light-curve (LC) width (Phillips 1993b), and SN color (Riess et al. 1996), which standardize the absolute peak magnitude of SNe Ia with a dispersion of ~ 0.12 mag ($\sim 6\%$ in distance; Betoule et al. 2014). However, with over 1000 well measured SNe Ia (Scolnic et al. 2018) each precisely photometrically calibrated to 2% (Lasker et al. 2019), systematics, and in particular astrophysical systematics now dominate the SNe Ia error budget (Betoule et al. 2014; Brout et al. 2019).

To address this, recent studies have focused on detecting, characterizing and exploiting correlations between SNe Ia and their environments. Such measurements provide an indirect route into the progenitor physics of SNe Ia, allowing for an improved understanding of the diversity and potential evolution of these SN. Studies in both the local universe and at high redshift have shown that the rates and properties of SNe Ia depend of host galaxy measurements such as galaxy morphology (Hamuy et al. 2000), stellar mass (Sullivan et al. 2010), specific star-formation rate (Smith et al. 2012), stellar population age (Rigault et al. 2018) and metallicity (Z; D'Andrea et al. 2011). Since all these galaxy parameters have been found to evolve with cosmic time, the properties of SNIa progenitors and, in turn, their ability to serve as a distance indicators may be affected by such evolution, which would add up to the systematic uncertainty budget.

Moreover, cosmological studies of SNIa have now firmly established a dependence of Hubble diagram residuals ($\approx$differences between distances estimated from SNIa peak brightness and those calculated assuming a fiducial cosmological model) on global host galaxy parameters, such as mass, age, and metallicity (e.g. Kelly et al. 2010; Lampeitl et al. 2010; D'Andrea et al. 2011; Gupta et al. 2011; Sullivan et al. 2010; Moreno-Raya et al. 2018). The addition of a term in the standardization of SNIa absolute magnitudes in the optical that accounts for these environmental properties (e.g. the 'mass step' or the γ-metallicity term; Moreno-Raya et al. 2016) has proved to further reduce the scatter of the Hubble residuals.

Most of these studies are based on analyses of the integrated or central host galaxy spectra, and broad-band or narrow-band Hα imaging. The effect of the local environment of SN Ia within galaxies in cosmological studies is almost unexplored. As an exception, Roman et al. (2018) presented an analysis of the dependences of SN light-curve parameters and Hubble residuals on their local environment using broad-band photometry. They show a significant dependence on the U-V color, which is treated as a proxy for the stellar age of the underlying populations (bluer being younger). However, age derived from photometry (color) has several uncertainties, and degeneracies (with extinction and stellar metallicity), and it is not enough to determine precisely the cut-out in stellar ages of such dependence.
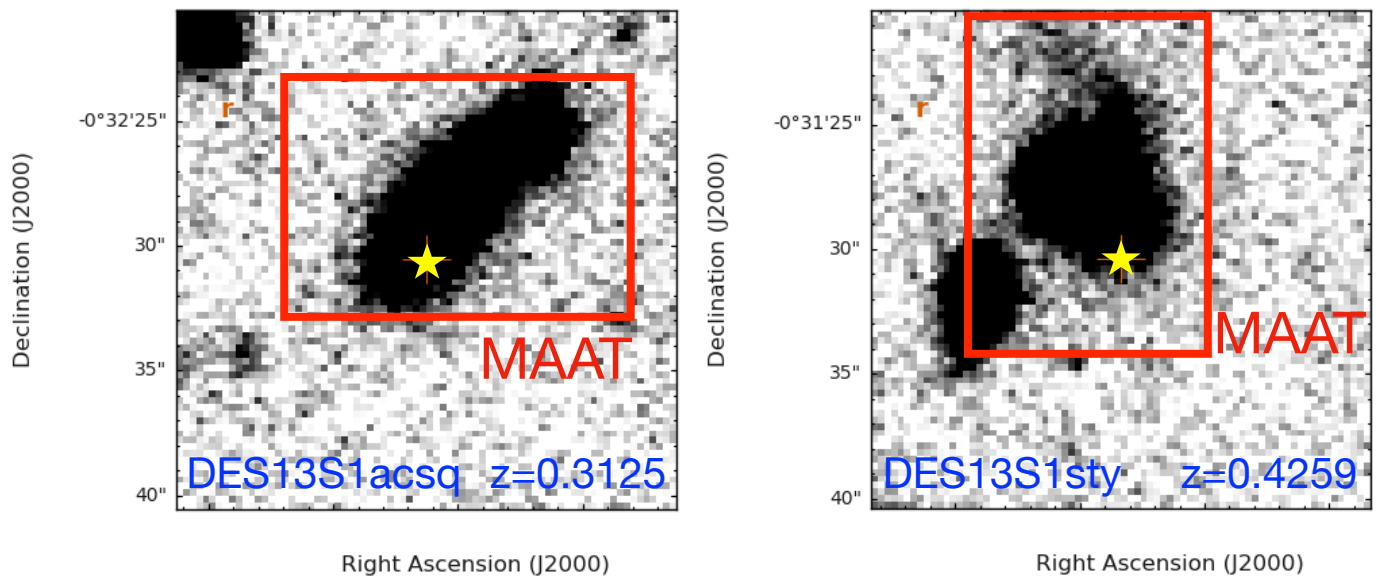
Figure 13. Twenty arcsec squared cutouts of SNe Ia DES13S1acsq and DES13sty discovered by the Dark Energy Survey at redshifts z=0.3125 and 0.04259, respectively. The yellow star is located at the SN location, and the red rectangle corresponds to the projected field-of-view of MAAT in the sky. With the GTC+MAAT configuration we will be able to spatially-resolve the SN environment in the galaxy and, at the same time, provide both global and local parameters. Cutouts courtesy of Philip Wiseman (priv comm., but see Wiseman et al. 2020).

Recent studies of SNIa host galaxies observed with integral field spectroscopy (IFS) have opened a new window in the field. For instance, Rigault et al. (2013, 2018), using observations of around a hundred very nearby host galaxies from the Nearby SN Factory (Aldering et al. 2002), showed that SNe Ia exploding at locations with higher star-formation intensity and higher specific star formation density could be more standardizable than those in passive local environments. In the last few years some efforts have been focused in compiling a statistical sample of SNIa host galaxies observed with IFS to probe this and other unexplored correlations with the local environment at low redshifts (z≲0.1; Kuncarayakti et al. 2013a,b; Galbany et al. 2014, 2016a).

There are currently a few instruments with the needed capabilities to perform such studies. While wide-field instruments allow to cover in full or at least large extents of host galaxies, high-spatial resolution is also needed to properly sample different regions of a galaxy including the location of the SNIa. In the Southern hemisphere, MUSE mounted to the 8.2m Yepun UT4 Very Large Telescope (VLT) and KOALA at the 4m AAT, are the best-suited instruments available. While MUSE is currently the only instrument combining the highest-spatial resolution (0.2" spaxel) with the largest FoV (1 sq. arcmin), it lacks of coverage of wavelengths bluer than ∼4650 Å(see e.g. Galbany et al. 2016b for an analisys of SN environemnts with MUSE). In the Northern hemisphere, PMAS mounted to the 3.5m telescope at the Calar Alto Observatory, is currently the only instrument available to perform such SN environmental studies. Stanishev et al. (2012) with their pilot work, and Galbany et al. (2018) later compiling the largest sample of nearby SN host galaxies observed with IFS (∼400; PISCO), have demonstrated the capabilities of this configuration.

At high-redshift, galaxies are both smaller in size and fainter, so ideal instruments do not need large FoVs but to be attached to either a large-aperture telescope or a satellite. In addition, the usual features used to characterize the main properties of galaxies (e.g. strong emission lines, like H Balmer lines) have shifted to near-infrared (NIR) wavelengths. KMOS at the 8.2m Antu UT1 VLT employs 24 small (8sq arcsec) integral field units with a configurable location within a field of ∼7 sq. arcmin and with a spatial resolution of 0.2 arcsec per spaxel, that provide IFS in the NIR. In the near future the James Webb Space Telescope (JWST) with its IFS NIRSpec will provide even a better configuration (9sq arcsec, with 0.1" per spaxel) from the space, at the price of having to observe on single object at a time.

Having the low-z (z≲0.1) and the high-z (z>0.5) ends covered, there is currently no instrument that is suitable for studying intermediate redshift galaxies. Ideally, it would need to combine a FoV large enough to cover the extent of galaxies at this redshift range (∼10-20 arcsec side), it would need to be mounted to a large-aperture telescope, and it would need to provide coverage in optical wavelengths up to 1nm. MAAT mounted at GTC would satisfy these three

requirements. In Figure 13 we show the locations (yellow stars) of two SNIa at intermediate redshifts from images obtained by the Dark Energy Survey (DES; Bernstein+2012). DES has compiled the largest, homogeneously identified sample of SNe Ia across cosmic time, with ~ 600 spectroscopically classified SNe Ia and ~ 2000 photometrically classified events to z=1.2. In the next few years, DES will produce the most stringent constraints on the nature of 'dark energy' prior to LSST. The red rectangle represents the projected field covered by one MAAT pointing, which fits perfectly well the size of galaxies at these intermediate redshifts.

Combining past and current efforts to compile a large smaple of low- and high-z SNIa host galaxies with PMAS/MUSE/KOALA and KMOS/JWST, we propose to use MAAT to obtain IFS observations of intermediate-z host galaxies of SNIa from the Dark Energy Survey. This will allow us to fill the redshift desert that in unexplorable with current instrumentation, and complete the studies of evolution of SNIa properties in a wide range of redshifts.

3.7. *Exploration of host galaxy environmental dependencies of Type Ia SN luminosities*

In recent years, H_0 measurements are achieving remarkable accuracy and precision thanks, in particular, to the use of distance indicators in the local Universe, but among all the local distance indicators, type-Ia supernovae (SNe) remain the most sensitive probe to estimate H_0. However, SN-Ia distances rely on primary distance indicator measurements; methods generally based on strong correlations among observational quantities, like the period-luminosity observed for Cepheids (Riess et al. 2019) or other indicators like the tip of the Red Giant branch inferred from observations of multiple stellar populations in SN-Ia host galaxies (Freedman et al. 2019). Once we have the possibility to use a calibrator sample for SNe Ia, we can use some proposed relations among their light curve properties and luminosity that are then calibrated with the primary indicators in order to measure the absolute luminosity and the distance of SNe Ia at larger distances (in particular at high redshifts).
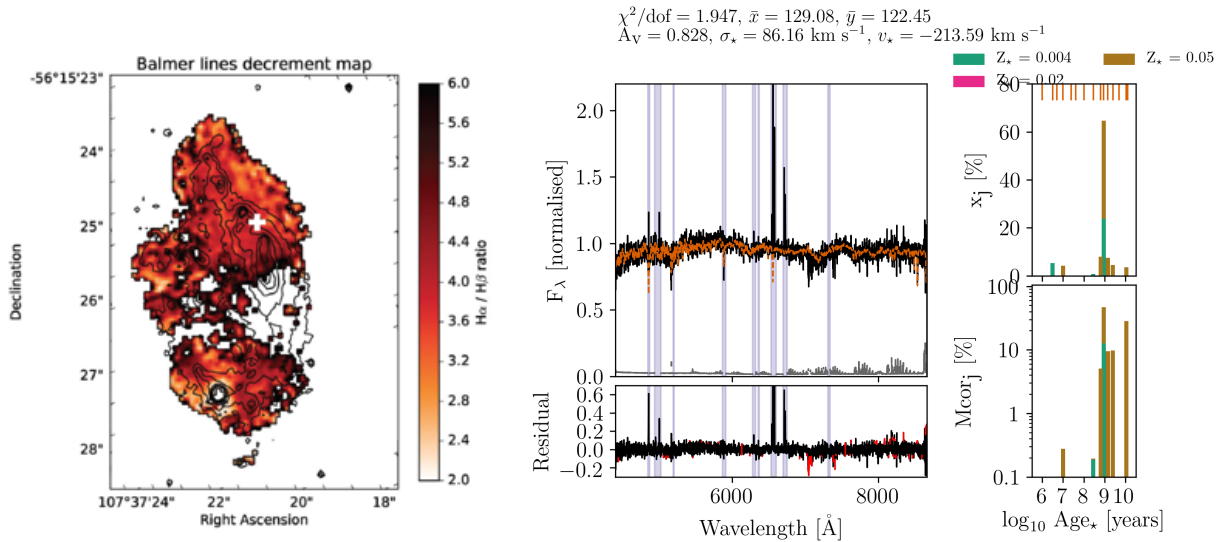
Figure 14. Left: The distribution of the color excess E(B-V) obtained from the Balmer decrement ratio for the case of the host galaxy of GRB 100316D (Izzo et al. 2017). The white cross corresponds to the location of the GRB. Right: The analysis of the region surrounding GRB 100316D (Izzo et al. in press) using the STARLIGHT (Cid Fernandes et al. 2013) spectral synthesis code. The left panels show the observed spectrum (black line) and the synthetic spectrum obtained from a combination of stellar spectra, whose eigenvalues (depending on the ages and metallicities of the eigenvector stellar spectra) are shown in the right panels. The lower left panel shows the residual spectrum, which is the nebular component at the GRB location.

The light observed from SNe-Ia is also affected by reddening from dust in their host galaxies. The change of color is a complicated correlation and an improper correction for reddening can lead to differences in the inferred SN luminosity, with important effects on the estimated cosmological parameters using these powerful distance indicators. There are several ways to estimate the amount of local dust in the host galaxy. 1) the Balmer decrement, the emission line flux ratio $H\alpha/H\beta$ at the SN position, which for typical nebulae conditions (case B, Osterbrock & Ferland 2006) is ~ 2.86, and deviations from this value are correlated with dust attenuation; 2) the spectral fit of the integrated stellar continuum of the underlying stellar population can provide an estimate of the wavelength-dependent attenuation, using

dedicated techniques based on the use of stellar population synthesis codes (Cid Fernandes et al. 2013; Eldridge et al. 2017); 3) in some cases, it is possible to infer the extinction through analysis of intervening interstellar absorption lines. Some of these lines, such as the Na I and K I resonance doublets or some DIBs like the 5780 $\mathring{A}$, seem to be correlated with the amount of gas along our line of sight to the SN (Munari & Zwitter 1997; Phillips et al. 2013).

The light from external galaxies is mainly composed by stars, in addition to the gaseous and dust components. However, the stellar populations responsible for the observed light are more mixed, which implies additional uncertainties on the real composition in terms of stars. In order to reveal the physical properties of the stars underlying a given region in a galaxy, which can be the location where a SN-Ia was observed, we must deal with a larger set of star formation histories with composite populations and with different stellar evolutions. IFS observations provide an enormous support in this research field, since we can study at high spatial and spectral resolution the immediate environments of SNe-Ia and the spatially-resolved global properties of the galaxy. This procedure is partly similar to what was proposed in the science case 1, about the study of kilonova environments. In the following, we describe the methods in detail, focusing for this specific case on the estimate of the host galaxy extinction value.
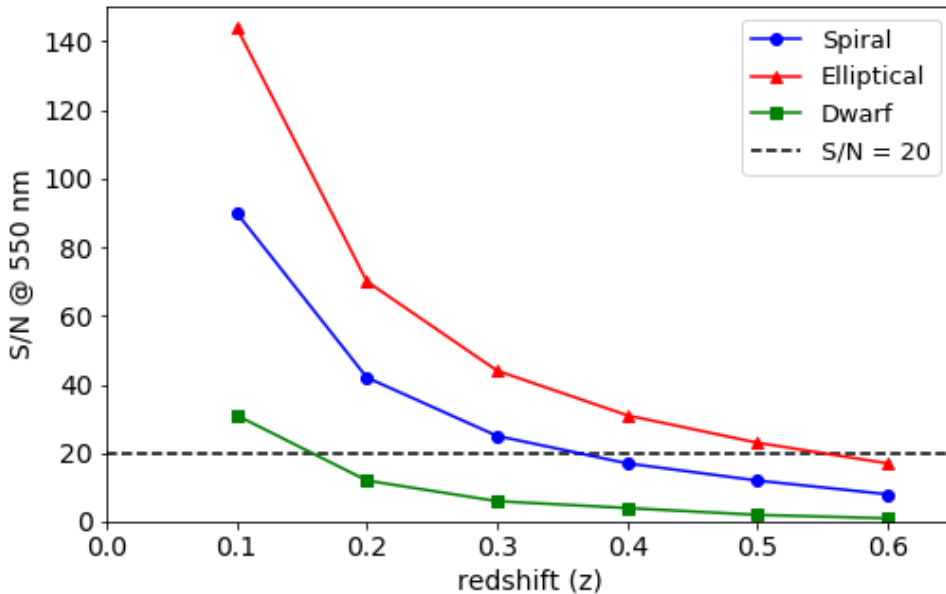
Figure 15. Our simulation of the distribution of the signal-to-noise of spectral region, computed at the wavelength of 550 nm, for different SN-Ia host galaxies as observed by MAAT@GTC. The black dashed line corresponds to our threshold for the signal-to-noise value, useful to obtain reliable results from stellar synthesis population analysis.

Each MAAT data cube will be analysed adopting a well-known strategy used for the study of stellar populations in distant galaxies. After defining a strategy for data binning, which can be based on optimising the signal-to-noise for each spectrum or on the study of single HII regions for star-bursting galaxies, we will use dedicated codes capable of decomposing each single spectrum in terms of different ages and metallicities of the underlying stellar populations. This technique is based on the use of a pre-defined stellar libraries, with stellar spectra of different ages and metallicities that represent the starting "eigenvector" base for the final decomposition analysis. After finding the best solution for each spectrum/region, we can finally provide estimates for the main physical properties like the extinction. An example of the application of this method to a GRB-SN host galaxy is shown in Figure 14. In the right panel it is shown an example of the decomposition of a spectrum through a pre-defined library of spectra with given ages and metallicities and how to obtain the residual nebular component, while in the left we display the distribution of the color excess E(B-V) obtained from the Balmer decrement.

MAAT@GTC can observe SN-Ia host galaxies at moderately high-redshifts, with the main goal of disentangling the stellar from the nebular component thus resolving the main emission lines (HI, [O II], [O III], [N II], [S II], He) in order

to obtain estimates of different physical properties such as metallicity, star-formation rate, ionisation, stellar ages and the extinction using both methods described previously. The SN Ia targets will be selected from the recently-released catalog of low-to-intermediate redshifts ($z = 0.0181 - 0.165$) SNe Ia discovered and monitored by the ZTF survey (Yao et al. 2019). This catalog contains 127 spectroscopically-confirmed type-Ia SNe with very high quality light curve data and all of them visible from La Palma. Considering 1 hour of observing time per SN, we can split our program in four observing semesters; in each one we will observe ~ 25 SN host galaxies in order to have a complete sample of SN Ia hosts after two years from the start of the program.

Moreover, SNe-Ia are observed in different types of galaxies. We have then simulated the signal-to-noise per spectral bin of MAAT, considering an average spatial sampling of $0.6'' \times 0.6''$ that takes into account atmospheric effects (seeing), for different host galaxies of SNe-Ia and a total exposure time of 1 hour using a combination of the R1000B and R1000R grisms. In this specific case we have assumed three types of galaxies: 1) a late-type Sa spiral with absolute magnitude $M_V = -18$ mag. Results are shown in Figure 15, considering a signal-to-noise (SN) value estimated at 5500 Å. Spectral decomposition can provide very good results if the spectra to be decomposed are characterised by a signal-to-noise of ~ 20. We then conclude that we can estimate physical parameters of the immediate environment surrounding a SN-Ia location in its host galaxy up to redshifts $0.5 - 0.6$ for an elliptical galaxy, $z = 0.2 - 0.3$ for spiral hosts and z=0.1 for dwarf host galaxies. We further notice that we did not assume any spatial averaging, which will increase the value for the signal-to-noise for each single case. However, spatial averaging implies that the region covered by each single spectral region will be much larger, an effect that depends also on the distance and not only on the spatial sampling. This can have some drawbacks, given that for a larger spatial region inside the SN-Ia host galaxy we would observe a combination of multiple stellar populations, which can slightly affect the value of the extinction at the location of the SN-Ia as inferred from stellar synthesis analysis.

3.8. Accurate binary masses with MAAT

One of the most important astrophysical parameters to be determined is the mass of an object, be it a star, a planet, a brown dwarf, or a stellar remnant (neutron star, black hole, white dwarf). For all but a handful of special cases, this is only attainable for objects belonging to binary systems, in which instance, it is essential to derive a spectroscopic orbit with the highest precision. For systems with very short orbits (with an orbital period of a few minutes to a few hours, i.e those that will likely merge, producing transients or gravitational waves), the need to sample well enough the orbit imposes tight constraints on the exposure time. When the primary is relatively faint (e.g., brown or white dwarfs, highly extincted or extragalactic systems), the use of échelle spectrographs is not feasible and one needs to rely on low- and intermediate-resolution spectrographs attached to large telescopes. It is thus essential to ensure that the highest radial velocity accuracy can be achieved by such instruments.

A good example of the need for high-efficiency, intermediate-resolution spectroscopy on 10-m class telescopes comes in the form of the binary central star of the planetary nebula Henize 2-428. GTC-OSIRIS longslit spectroscopy allowed Santander-García et al. (2015) to derive a double-lined spectroscopic orbit of the star (while similar observations with FORS2 mounted on the VLT did not provide sufficient signal-to-noise, highlighting that these observation are on the limit of current GTC capabilities). The radial velocity curve combined with photometric observations from smaller facilities indicated that the system was a double degenerate with total mass exceeding the Chandrasekhar limit and, thus, the strongest known candidate type Ia supernova progenitor. Recent work has begun to indicate that at the resolution of GTC-OSIRIS the principal spectral lines used by Santander-García et al. (2015) might be blended with absorption associated with diffuse interstellar bands (DIBs; Reindl et al. 2019), hindering the accurate measurement of radial velocities – in this case possibly leading to over-estimating the component masses. The increased efficiency and resolution provided by MAAT would allow these lines to be resolved from their contaminants, and thus could prove crucial in unravelling the mystery of the origins of supernova type Ia (Rebassa-Mansergas et al. 2019).

Another important example of the possible contribution that MAAT would provide comes in the field of black hole binaries. Black hole binaries are studied as single-lined spectroscopic binaries where the mass ratio is derived by measuring the radial velocity curve and projected rotational broadening of the companion star, the latter having typical values $\sim$40–100 km s^{-1} depending on orbital parameters. The capabilities of OSIRIS have already been pushed to their limit in this field, via the use of extremely narrow long slits (Torres et al. 2020) where MAAT would offer a clear advantage in measuring both the radial velocity variations and rotational broadening, as well as allowing for measurements to be made for fainter, more distant systems. The black hole mass distribution that will be obtained

from Galactic binary systems using MAAT will improve our understanding of their formation mechanisms, as well as the origin of the black hole mergers detected with gravitational wave detectors.

According to Gustafsson (1992), the uncertainty on a stellar radial velocity measurement (σ_{rv}) is inversely proportional to the signal-to-noise ratio (S) of the spectrum as well as the resolving power (R) of the spectrograph to the power of $3/2$, i.e. $1/\sigma_{rv} \propto R^{3/2}S$. As such, the increased efficiency of MAAT with respect to a typical OSIRIS long-slit (which, at 0.6", generally implies significant slit losses) directly leads to an improvement in radial velocity precision. Furthermore, the increase in resolution again leads to a substantial improvement in radial velocity precision.

Using MAAT will typically lead to an increase in resolution by $\sim$60% and increase in observed flux by $\gtrsim$20% over OSIRIS with the 0.6" long-slit – this results in a gain of a factor 2.2 in terms of radial velocity precision (i.e. $\sigma_{\mathrm{MAAT}} \sim 0.45\sigma_{\mathrm{OSIRIS}}$). Furthermore, this should be considered a *minimum* gain as MAAT will maintain this precision even in poor seeing conditions (where OSIRIS slit-losses could become untenable), and MAAT removes any risk of losses or systematic effects due to inaccurate centring.

We also highlight that a number of higher resolution VPH grisms have been designed for OSIRIS but were never constructed – each of which would push the MAAT resolving power up to 8,000. With the designs available, the only associated costs would be for production. The inclusion of the construction of one or more of these gratings in the MAAT budget would greatly aid the final exploitation of the instrument – allowing for sub km s^{-1} precision measurements of the radial velocities of all but the faintest of sources (particularly around the strong Hα absorption / emission line).

3.9. *The abundance discrepancy in planetary nebulae with MAAT*

The "abundance discrepancy" problem is one of the major unresolved problems in nebular astrophysics, and it has been around for almost eighty years (Wyse 1942). In photoionised nebulae —both H II regions and planetary nebulae (PNe)— optical recombination lines (ORLs) provide abundance values that are systematically larger than those obtained using collisionally excited lines (CELs), the ratio between the two being the abundance discrepancy factor (ADF). Solving this problem has obvious and deep implications for the measurement of the chemical content of nearby and distant galaxies, as this is most often done using CELs from their ionised interstellar medium.

The reason of this discrepancy has long been a matter of debate (see García-Rojas et al. 2019) and no concensus has been reached today. Focusing on PNe, several spectroscopic studies have shown that the faint ORL emission is strongly enhanced in central regions of PNe with known close-binary central stars and high ADFs (e. g. Corradi et al. 2015; Jones et al. 2016; Wesson et al. 2018). These extreme ADFs have been associated with the presence of cold, metal-rich gaseous clumps in the nebula, which are very efficiently cooled by the heavy elements (Liu et al. 2000). The first clear evidence of two plasma components with a probable distinct origin was provided by García-Rojas et al. (2016), who found, using OSIRIS-GTC tunable-filter imaging of a high-ADF PN, that ORL and CEL emission had clearly distinct geometries. Having spatially resolved information of both the emission of these lines as well as of the physical conditions can reveal crucial information on the mass ejection modes of both plasma components. PNe with binary central stars and/or high ADFs are perfect targets to map the emission of both kind of lines, as well as the physical conditions obtained from several diagnostics, owing to the surface brightness of the usually very faint ORLs is large enough to be within the reach of large telescopes.

MAAT+GTC offers the opportunity of accessing high-spatial resolution 2D spectroscopy even in relatively faint lines, such as metal ORLs, and additionally covering the blue ($\lambda < 4600$ Å) range of the optical spectra, where some important diagnostic on the abundance discrepancy lie and therefore, address some interesting questions: i) to study if the spatial distribution of the electron temperature (T_e) sensitive [O III] $\lambda4363$ auroral CEL correlates with O II and/or O III ORL emission and, if so, quantify the effect on the determination of T_e and the ADF (Gómez-Llanos et al. 2020); ii) to map the spatial distribution of T_e derived from the Balmer Jump at $\sim$3646 Å that would give us an estimate of the spatial distribution of the T_e of the cold plasma component; iii) to study the recombination contribution to the nebular [O II] lines at $\lambda\lambda3726+29$ CELs in high-ADF PNe, which can make electronic density diagnostic from these lines unreliable (Wesson et al. 2018). It is worth mentioning that OSIRIS+MAAT would be the only instrument in a 10m-class telescope in the northern hemisphere providing simultaneously high-spatial sampling and a complete coverage of the optical wavelength range.

Finally, these kind of observations combined with kinematical information obtained from e. g. MEGARA, can provide strong constraints to 3D photoionization models and give crucial information to understand the physical mechanisms
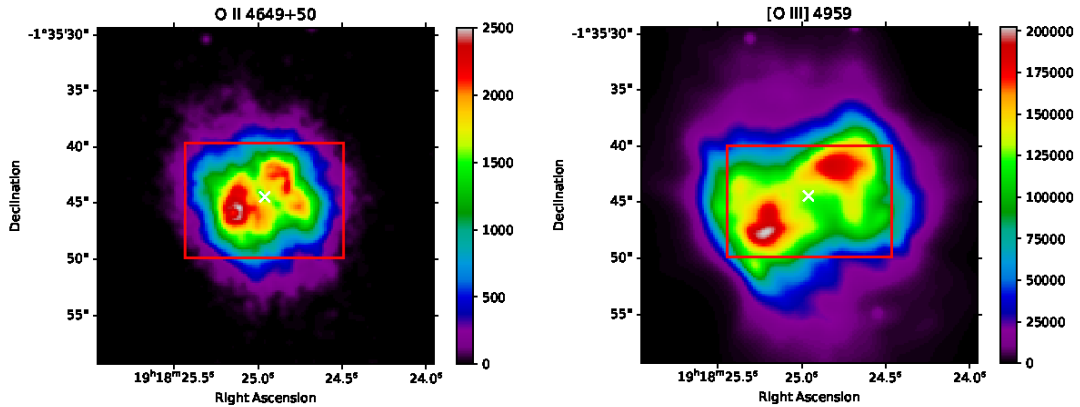
Figure 16. MUSE-VLT emission line maps of planetary nebula NGC6778 illustrating different spatial distribution of ORL and CEL emission in high ADF planetary nebulae. Left: O II $\lambda\lambda$4649+50. Right: [O III] λ4959. The red box show the FoV of OSIRIS+MAAT.

that are acting in the ejection of the metal-rich component. Summarizing, with the arriving of MAAT, the GTC would have a suite of instruments that can be of paramount importance for the topic of the abundance discrepancy problem.

3.10. *Brown dwarfs and planetary mass objects with MAAT@GTC*

Brown dwarfs were first confirmed unambiguously 25 years ago and nowadays they constitute a well recognized population in open clusters, young moving groups, star-forming regions and the solar neighborhood. Their properties provide a natural link between stars and planets. More recently, planetary mass objects have been recognized free-floating in the field and also as companions to stars. Their masses overlap between those of brown dwarfs and planets, and their formation mechanism is not yet understood.

The Euclid and the Vera Rubin LSST surveys will provide the next major source of discoveries of brown dwarfs and planetary-mass objects during this decade. Spectroscopic reconaissance of the candidates detected with those surveys will be in high demand. A strong synergy between Euclid, Vera Rubin LSST and MAAT@GTC presents itself to discover new bona-fide brown dwarfs and planetary-mass objects.

In particular, our simulations of the Euclid performance indicate that over 1 and half millions L and T dwarfs will be detected in the J-band (Figure 1). About 1% of them could be young planetary-mass objects. Thus, Euclid can potentially increase the known number of brown dwarfs and planetary-mass objects by about 2 orders of magnitude, but it needs complementary observations to characterize them efficiently.

A special science case that can be solved by the powerful combination of Euclid and MAAT@GTC data is the determination of the lithium depletion boundary among brown dwarf members in the Coma Berenices open cluster, the second nearest star cluster to the Sun. Using OSIRIS@GTC long-slit mode with the R1000R grating we have observed the faintest candidate L dwarfs in this cluster, investing over thirteen hours of observing time. The spectra allowed us to determine spectral types, measure radial velocities and search for the LiI resonance double at 6708 A (Figure 2). We were able to confirm the cluster membership of four brown dwarfs, but we failed to detect lithium. Using evolutionary models for brown dwarfs we impose a lower limit of 550 Myr to the age of the cluster (Martín et al. 2020, AA, submitted). In order to be able to find the resurgence of lithium in this open cluster we need to probe about one or two magnitudes deeper. Fainter brown dwarf candidates in Coma Berenices will be furnished by the Euclid wide survey, and we need to enhance the spectroscopic sensitivity of OSIRIS to search for lithium in those objects in a reasonable amount of observing time. Given the increase in spectral resolution provided by MAAT@GTC, we estimate that lithium could be detected using the R300R grating instead of the R1000R grating with the one arc second slit. Thus, we would gain a factor of three in sensitivity just by being able to use a lower dispersion grating.

Our final remark is that MAAT@GTC is a very welcome addition to OSIRIS which would arrive in a very timely period when we expect an enormous increase in the number of new brown dwarf and planetary-mass candidates that will need spectroscopic confirmation.

4. INSTRUMENT OVERVIEW

Simulation Results: Detection Counts by A. Burgasser

1-2M L dwarfs
0.5-1M T dwarfs
100k sdLs & 10k sdTs
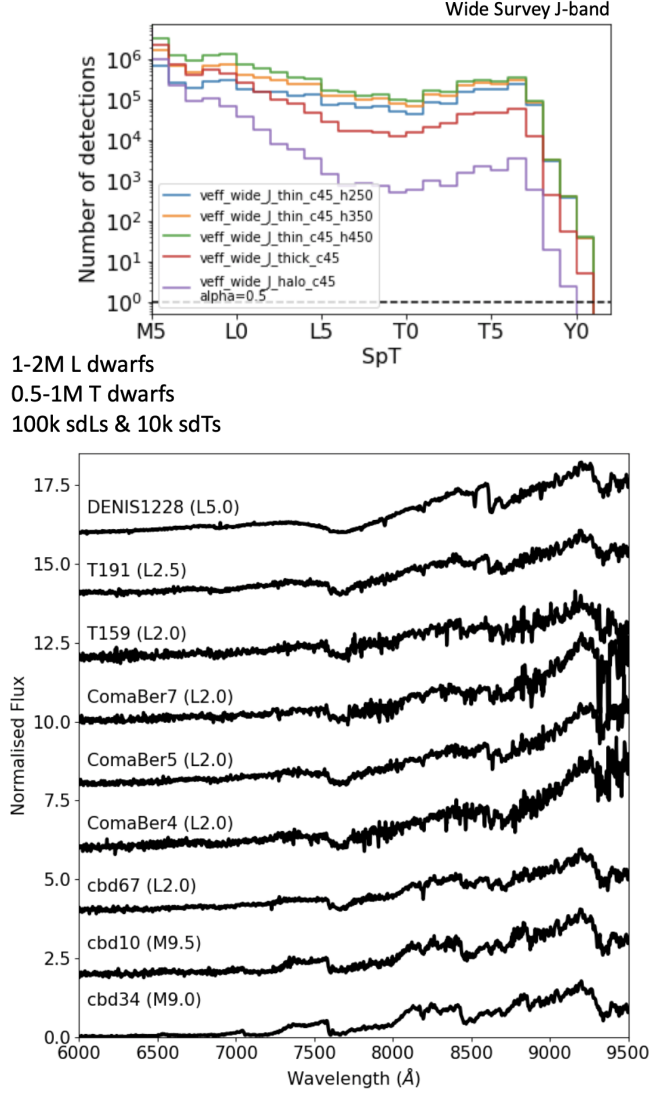
Figure 17. Top: .... Bottom: ...

In this section we describe the MAAT instrument in detail and the interfaces with OSIRIS. We provide its technical specifications and a complete description of its envelope, optics layout and parameters, overall throughput and performance, data simulations and pipeline overview, as well as the observation scheme with OSIRIS+MAAT. The engineering work presented in this proposal has been carried out in close collaboration with the staff at GRANTECAN (see Section **??**). The results of this study demonstrate that the construction of MAAT is feasible and meets the technical requirements for its installation on OSIRIS.

4.1. *MAAT on OSIRIS*

A realistic representation of the MAAT module (or box) is shown in Figure 18. This figure displays the space envelope of MAAT as result of the exhaustive mechanical and interfaces study done by the GTC staff (see Section 4.2 for details and dimensions). All IFU optical elements are located inside the MAAT box, which will be located in the space equivalent to six mask-frame slots. Thus, when the IFS mode of OSIRIS is required for observing, the MAAT module will be inserted into the telescope beam as if it were a slit-mask. A pick-off mirror inside the box directs the

light from the focal plane through fore-optics and onto the mirror slicer, and mirror elements, to reformat the focal plane into the pseudo-slit that passes the light into the rest of the OSIRIS spectrograph (see Section 4.3 for the optics layout and parameters). We want to emphasise that there are no moving parts, neither cables nor electronics, inside the MAAT module, i.e. MAAT is an optical module that, to all effects, is *seen* by the OSIRIS control system as another slit-mask frame. See Section 6 for the details of observing with OSIRIS+MAAT.
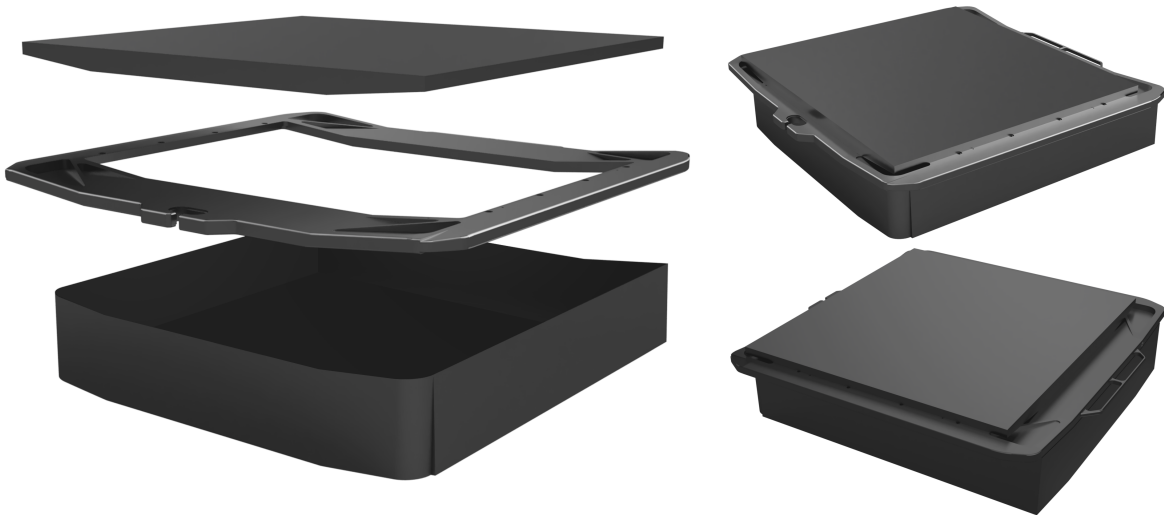
Figure 18. A realistic overview of the MAAT module based on the exhaustive space mechanical and interfaces study done by the GTC staff. The mask-frame (middle component in the left panel) is identical as that of any OSIRIS mask. Top and bottom directions points to M2 and OSIRIS respectively. The box has one entrance hole (not shown) for the IFU pick-off mirror on its surface pointing to M2. The surface pointing in the direction of OSIRIS will have the slit aperture.

The concept of the mirror slicer IFU for OSIRIS has been performed by our collaborator and optical scientist Robert Content at the Australia Astronomical Observatory. This has demanded a very detailed study and in depth understanding of the OSIRIS spectrograph, both as designed (by studying its Zemax ray-tracing optical design, see Figure 19) and as built (see below). We also had the collaboration of Ernesto Sánchez-Blanco (OpticalDevelopment), who implemented all OSIRIS Grisms and volume-phase holographic gratings (VPHs) in Zemax, since we initially had available only the optical design for imaging, but not for spectroscopy. Figure 20 shows the Zemax modeling of the OSIRIS suite of Grisms and VPHs respectively, which were integrated in the Zemax design model of OSIRIS for the MAAT optical development feasibility study.

MAAT will enhance the resolution power R of OSIRIS by 1.6 times with respect to its 0.6″ wide long-slit thanks to the 0.303″ width of each mirror slice. This is a best estimate and will depend on the correction of the spectrograph aberrations that can be done by the IFU re-imaging mirrors, especially the local defocus and astigmatism along the slit mask. Figure 21 shows the OSIRIS PSF for the slicer as compared to the long-slit. All the eleven OSIRIS Grisms and VPHs will be available to provide broad spectral coverage with moderate resolution (R=600 up to 4100) in the spectral range $360 - 1000$ nm. Table 3 lists the main parameters of all Grisms and VPHs for the new IFS observing mode of OSIRIS+MAAT.

The proposed IFS mode for OSIRIS with MAAT will take advantage of the expected significant increase in the overall OSIRIS efficiency due to its relocation at the GTC Cassegrain focus (a net gain of $\sim 10\%$ is expected in the total throughput by the removal of M3), and to its new monolithic e2v $4k \times 4k$ detector. For our studies we have adopted the CCD231-84 Back-illuminated Scientific Sensor with 4096×4112 pixels, each of 15 μm. See Figure 22 with
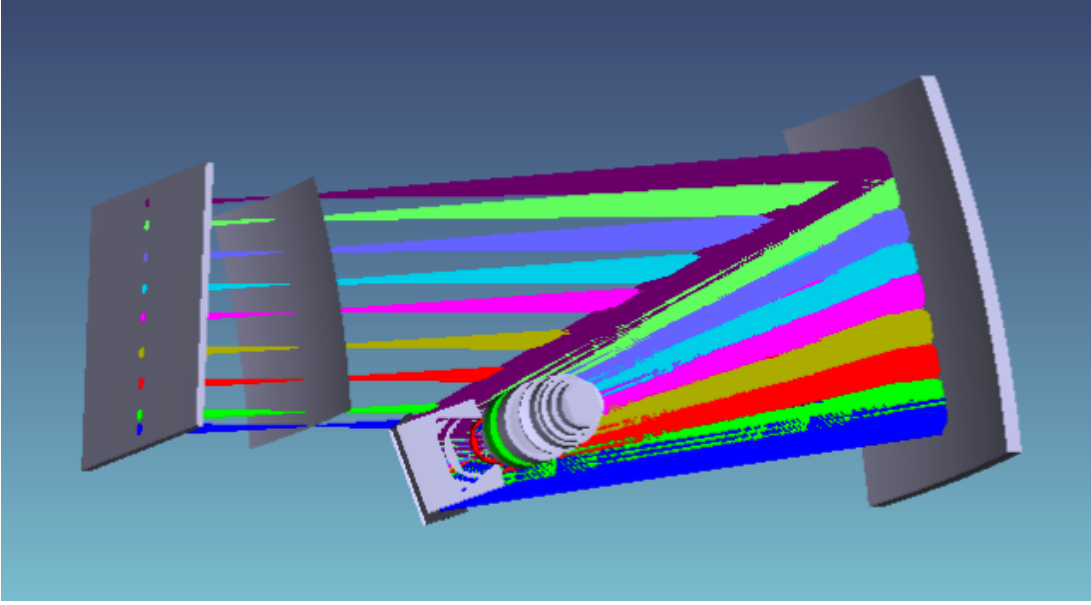
Figure 19. OSIRIS optical layout in spectroscopy mode.

Table 3. Resolutions and spectral ranges available with OSIRIS+MAAT for all available Grisms and VPHs

ID	λ_c (Å)	$\Delta\lambda$ (Å)	D (Å/pix)	R (LS[1])	Peak Efficiency	Type
R300B	4405	3600-7200	2.60	575 (360)	70%	Grism
R300R	6635	4800-10000	4.02	560 (348)	70%	Grism
R500B	4745	3600-7200	1.87	860 (537)	68%	Grism
R500R	7165	4800-10000	2.58	940 (587)	67%	Grism
R1000B	5455	3630-7500	1.13	1630 (1018)	65%	Grism
R1000R	7430	5100-10000	1.40	1795 (1122)	65%	Grism
R2000B	4755	3950-5700	0.46	3465 (2165)	87%	VPH
R2500U	3975	3440-4610	0.33	4090 (2555)	70%	VPH
R2500V	5185	4500-6000	0.44	4025 (2515)	80%	VPH
R2500R	6560	5575-7685	1.56	3960 (2475)	80%	VPH
R2500I	8650	7330-10000	1.73	4005 (2503)	80%	VPH

[1]Resolving power for the OSIRIS 0.6″ long-slit (LS) mode.

the characteristics of this new OSIRIS e2v detector and its spectral response compared to the two Marconi CCD44-82 (2048 × 4096 pixels) mosaic (with 37 pix binned gap between them) currently installed on OSIRIS. MAAT has been conceived and designed to take advantage of both actions, which will be completed by the end of 2021.

4.2. *MAAT envelope study*

We summarise in Table 5 the main MAAT envelope technical specifications. The 2D drawing with the detailed dimensions of the space envelope of the MAAT module is displayed in Figure 23. All details are also available in the *.step* file provided by GTC, which 3D-view is shown in Figure 18.
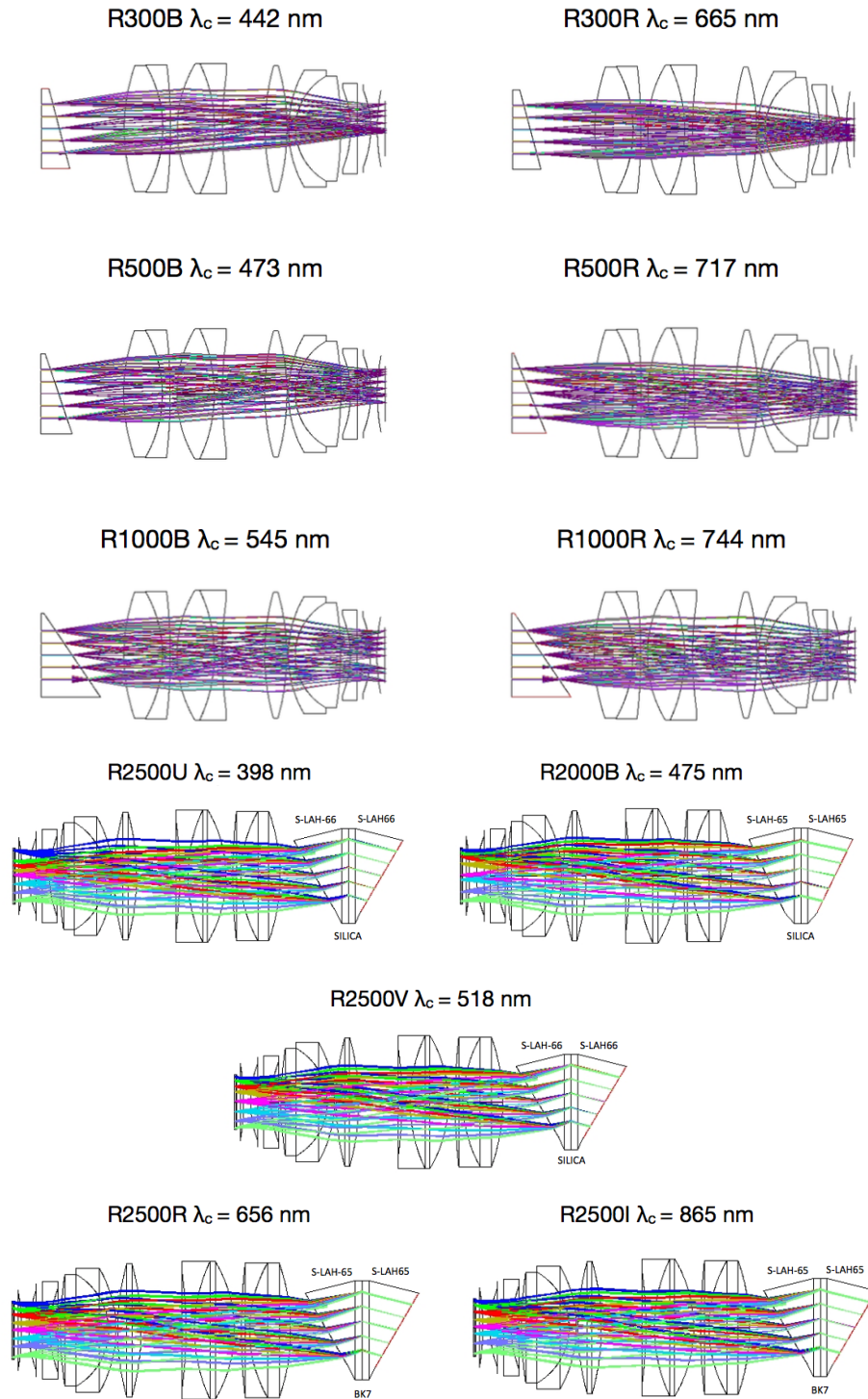
Figure 20. Top: Zemax ray-tracing models of the OSIRIS suite of Grisms. Bottom: The same for the suite of VPHs.

The MAAT box will be inserted inside the OSIRIS Slit Subsystem shown in Figure 24. The MAAT box space envelope takes up the space equivalent to 6 masks in the OSIRIS masks Charger. The location of MAAT inside the OSIRIS Charger would be around the central position, leaving space to the left for 4 masks and to the right of MAAT for another 3 masks, i.e. a total of 7 masks will be reserved for OSIRIS standard observation modes (long-slit, MOS,
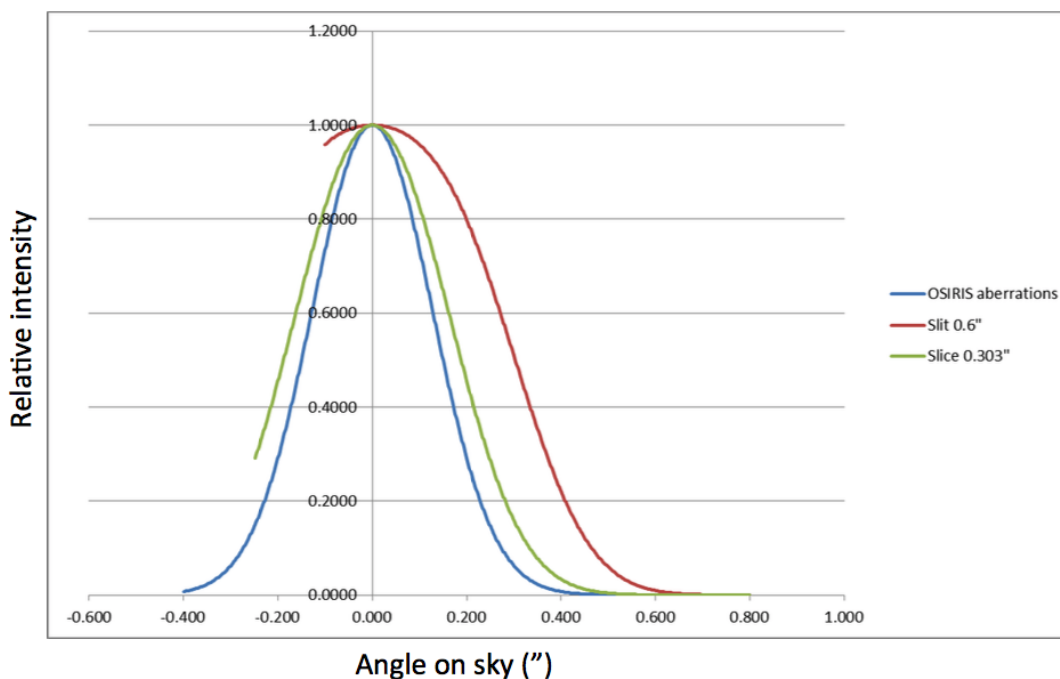
Figure 21. PSF of OSIRIS for the MAAT slicer width of 0.303″ as compared with the 0.6″ wide long-slit. OSIRIS aberrations were assumed to be a Gaussian 0.3″ FWHM. This is larger than the as-designed aberrations given by Zemax to take into account mechanical errors as alignments.

Figure 22. Left: Characteristics of the new OSIRIS e2v CCD231-84 detector. Right: Spectral response of the new OSIRIS e2v CCD231-84 (red) compared to the current Marconi CCD44-82 (black)

calibrations). Figure 24 shows also a picture of the OSIRIS Cartridge and focal plane assembly as built. The figure seems to show that in the upper part of the Mask Loader mechanism there is no range due to the proximity to the masks edge protection (in yellow color). This element is used to retain the masks when the instrument rotates. This hypothesis does not apparently become true when the MAAT envelope is introduced into the OSIRIS focal plane, since the masks edge protection seem not to interfere with the focal plane (to be confirmed when insertion tests could
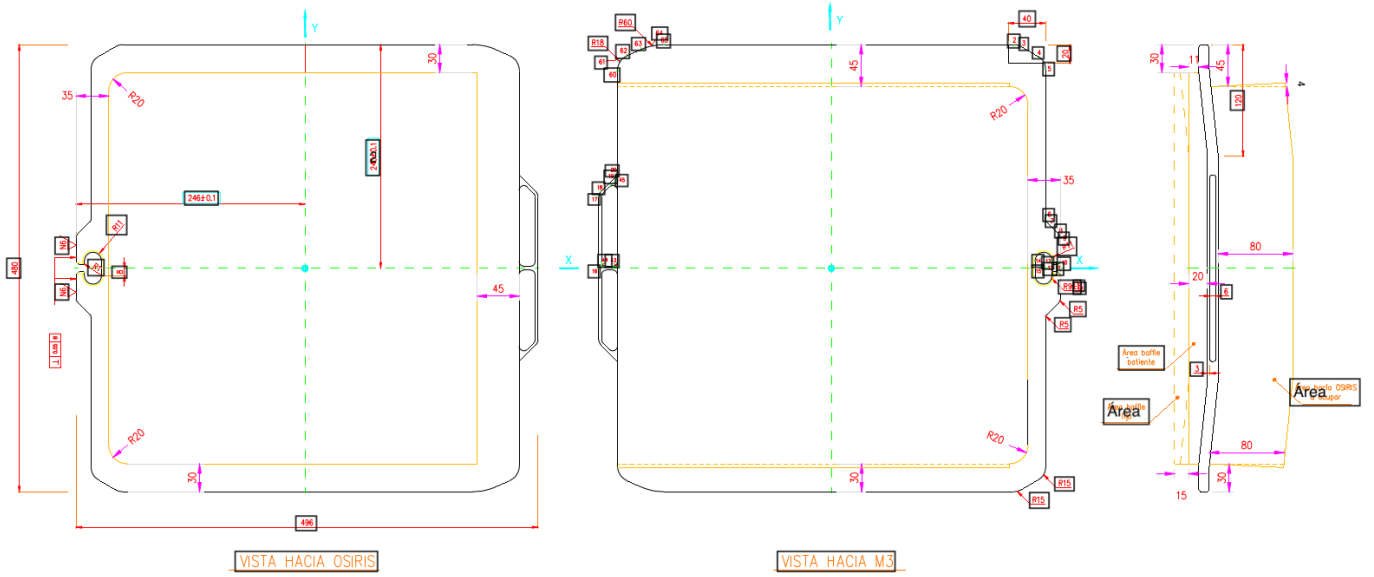
Figure 23. 2D drawing of the MAAT space envelope with dimensions (Credit: GTC).

Table 4. MAAT envelope technical specifications

Parameter	Value
Spectrograph focal plane radius[1]	1814 mm
Focal plane sag along slit[2]	11.07 mm
Slit length[3]	400.2 mm
Angle slit vs. OSIRIS optical axis[4]	4.16 deg
Space envelope	X: 405 mm
	Y: 441 mm
	Z: 112 mm
Weight[5]	10 Kg

[1] Edges toward the telescope.

[2] Edge to slit centre.

[3] Ignoring curved focal plane.

[4] As in the OSIRIS Zemax.

[5] Maximum weight load of the entire MAAT box (to be confirmed, see text).

be done). Secondly, it appears that the metal baffle (grey colour) does not stop the MAAT envelope from being positioned into the focal plane. Finally, the third element is the mechanical support baffle (in green and red colour), which certainly avoid the insertion of the MAAT envelope into the focal plane, reason why there would be to redesign a wider structure baffle that would allow the MAAT envelope width fit the baffle dimensions. The final confirmation of these three elements is pending until the insertion masks test could be done, which means de-mounting the mechanical support baffle (green/red colour).

The GTC staff has 3D printed two dummies to simulate the MAAT envelope (see Figure 25) to be tested *in situ* on OSIRIS. Figure 25 shows several pictures of the dummy of MAAT as inserted in its nominal position inside the
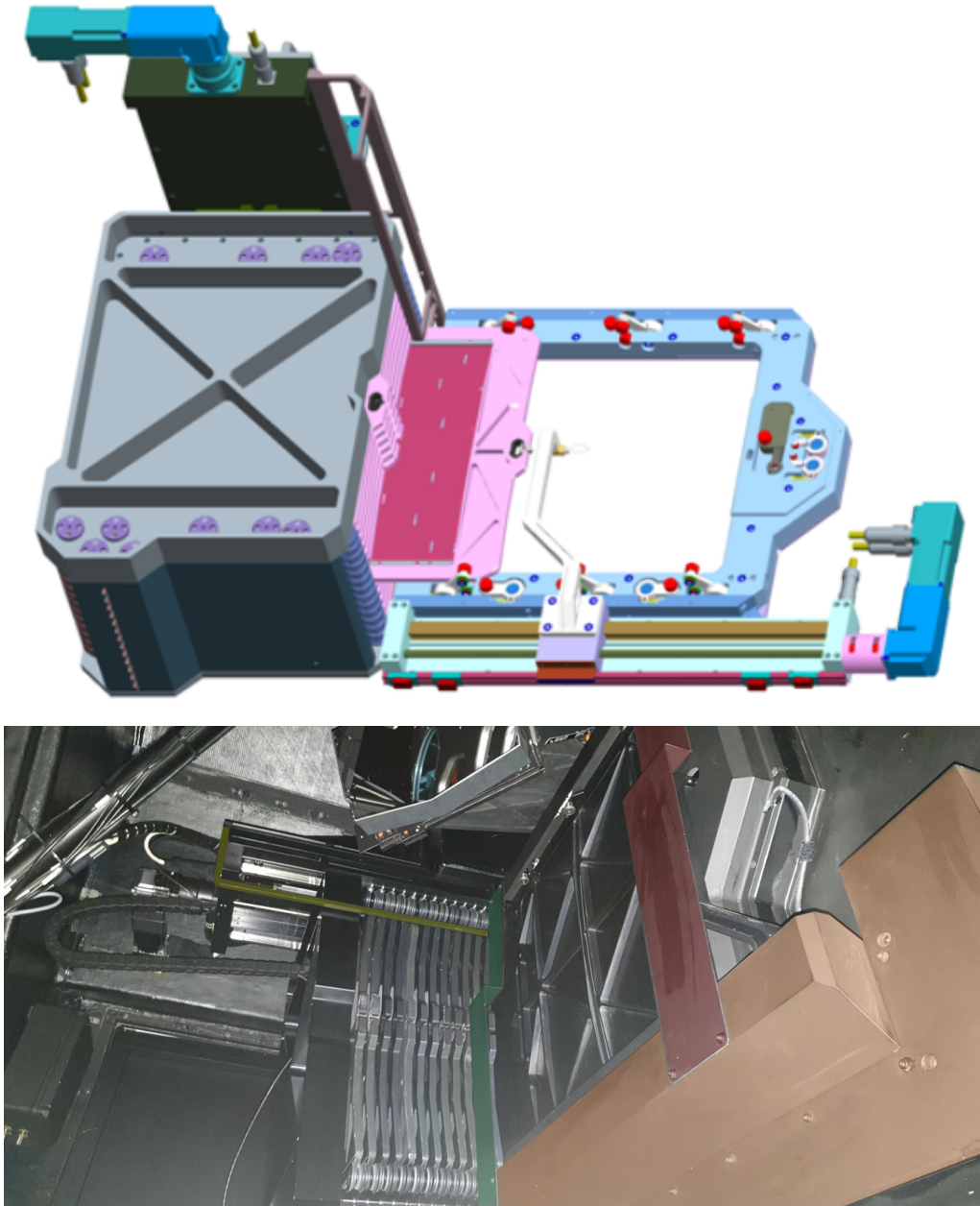
Figure 24. Top: Model view of the OSIRIS Slit Subsystem without baffle, consisting of a Jukebox (on the left in gray), with a capacity of 13 masks and a Charger, on the right in blue, which inserts the mask (in pink) selected by the control on the plane focal length of the telescope (Credit: GTC). The MAAT box will be inserted in the Jukebox and occupies the equivalent to 6 masks (see text). Bottom: Picture of the OSIRIS Cartridge and focal plane assembly as built. We highlight in color different metal pieces: yellow for the masks edge protection, green and red baffle for mechanical support and as baffle (see text for more details). To all effects, the MAAT box will be inserted in the focal plane of OSIRIS when required as if it were another long-slit mask (Credit: GTC).

OSIRIS Jukebox. These tests were performed on January 14, 2020 and have demonstrated that the MAAT assembly fits well into the Cartridge, without interference with the lower and upper shaft cam rollers neither the adjacent masks units. The tests need to be completed by inserting the MAAT module into the focal plane of OSIRIS. All indicates that everything should work out well.

To all effects, the MAAT module will be placed in the focal plane of OSIRIS when required as if it were another mask (see Figure 26). The OSIRIS Mask Loader Mechanism allow us to remove the selected mask, in this case the

Figure 25. Top: 3D printed dummies built for the *in situ* testing of the MAAT envelope on OSIRIS (Credit: GTC). Bottom: *In situ* testing of the dummy of the MAAT module on OSIRIS: a) MAAT envelope dummy placed in the Loader mask, b) Baffle to redesign in order to accomodate the subsystem mask frame plus MAAT envelope, c) Width of the MAAT envelope, d) Free space between the rollers and the lower part of the MAAT envelope (orientation $rotB = 80°$), and e) Free space between the upper part of the MAAT envelope and the masks edge protection (orientation $rotB = 80°$). All these pictures have been taken with orientation of $rotB = 80°$. (Credit: GTC).

MAAT box, from the Cartridge and place it in the correct position of the Loader. It also allows to put it back in the Cartridge when needed. It moves by means of a brushless motor, which coincides with the number 1 motor of the PMAC#1 controller, assigned to the control of the $X-$axis movement. The motor (and drivers in the associated control part) is a Parker model SM232AD. Currently, the motor / encoder rotates at 2000 counts per lap. In principle the motor should be able to retrieve up to 10 kg, which should be sufficient to handle the MAAT module. Yet, this
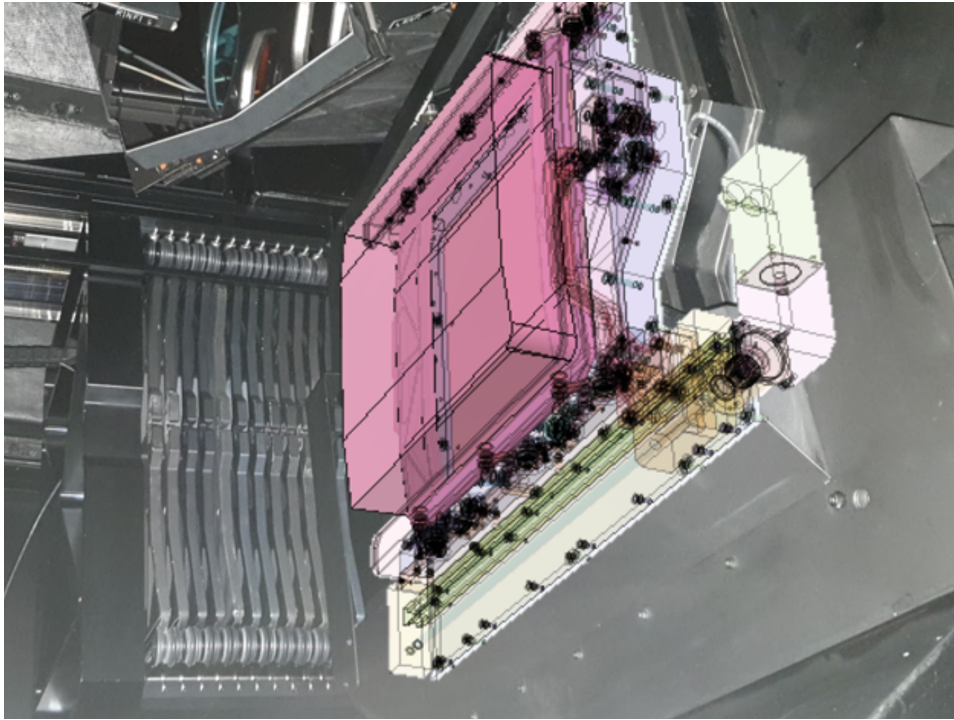
Figure 26. The MAAT box has been placed on the OSIRIS focal plane. (Credit: GTC).

will have to be tested with a dummy to make sure that we do not put the motor under stress. Since the separation between two consecutive positions in the Cassette is 20 mm, it is necessary to move the encoder 80,000 beads to move from one discrete position to the next. Thus, the Table of discrete positions with respect to the "home" position will have to be updated to include the MAAT box in replacement for the equivalent to 6 OSIRIS masks.

Another critical aspect of the envelope study has been the understanding of the optical vignetting due to the OSIRIS collimator mirror support (and filter wheel). This feature is not present in the OSIRIS Zemax model as designed. However, it is a well known feature that our colleague Robert Content has studied very much in detail by looking at real OSIRIS images to map the vignetting pattern (see Figure 27). In this figure we also mark the position of the OSIRIS long-slit which is at the same location as that of the pseudo-slit of the MAAT IFU. In practice, we designed the IFU in such a way that we maximise the Field-of-View of the IFU, allowing a very minor vignetting in the top-left corner of the MAAT sky footprint (see Figure 2). More details are given in the section below. For our understanding of the exact location of the OSIRIS and GTC optical-axis on the correspondence between the OSIRIS long-slit masks on the OSIRIS CCD the mapping shown in Figure 28 has been extremely relevant for the development of the IFU optical concept.

4.3. *MAAT optics layout and parameters*

The proposed MAAT optical solution is based on the concept of Advanced Image Slicer (AIS) developed by Robert Content whom has designed the most relevant AIS-IFU optical systems in ground-based 10-m class telescopes and space projects up today. As examples this includes the designs of the MUSE mirror-slicer IFU (Henault et al. 2004), the KMOS mirror-slicer system (Content 2006), the Gemini GNIRS slicer (Content 1998), and the JWST NIRSpec slicer (Content 2000). For completeness we should also mentioned his Gemini GMOS-IFU (Allington-Smith et al. 2000) and Magellan IMACS-IFU (Schmoll et al. 2004) designs using fiber-lenslets. We are also in close contact with the company Winlight in Marseille who are well recognised for the optical manufacturing (including opto-mechanics) of the MUSE and KCWI mirror-slicer IFUs (see Figure 30), among others, and complete spectrograph systems such as MUSE, DESI, and PFS. The results presented here support the feasibility of MAAT. Naturally this work will have to evolve into proper and formal phases of Conceptual, Preliminary and Final design for the eventual construction of MAAT (see Section 7). At this stage of the project we do not address the optomechanical aspects of the IFU optical
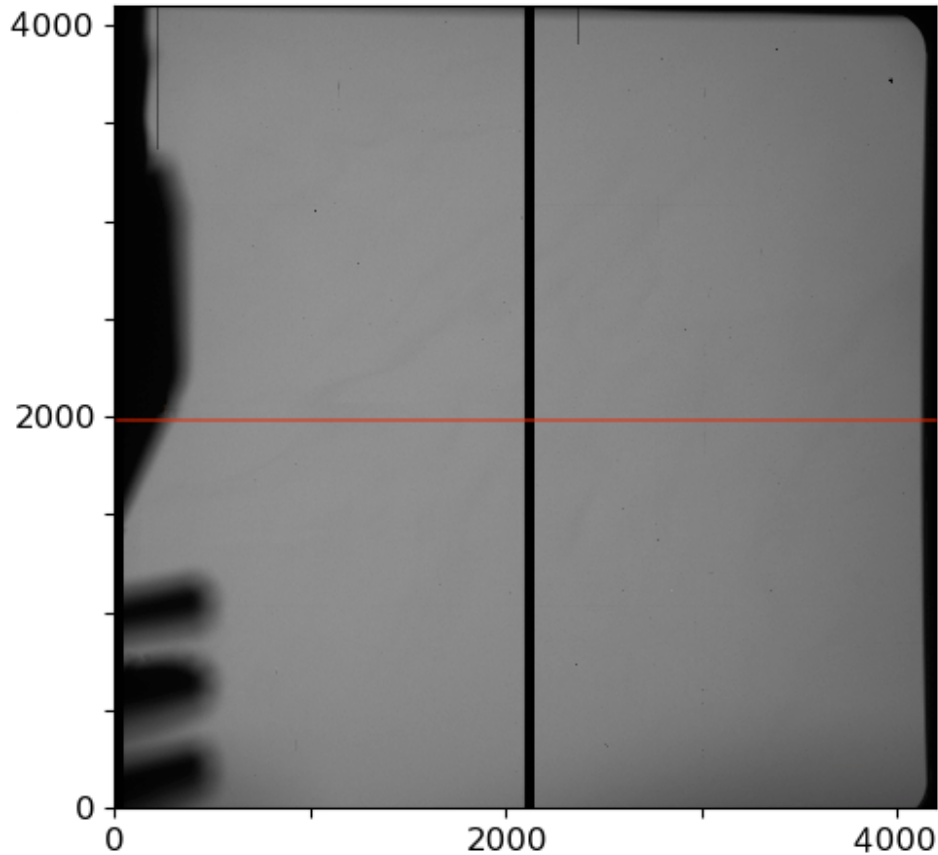
Figure 27. Vignetting pattern as seen in an OSIRIS image. The red line marks the correct position of the OSIRIS long-slit, which we adopted for the IFU pseudo-slit.
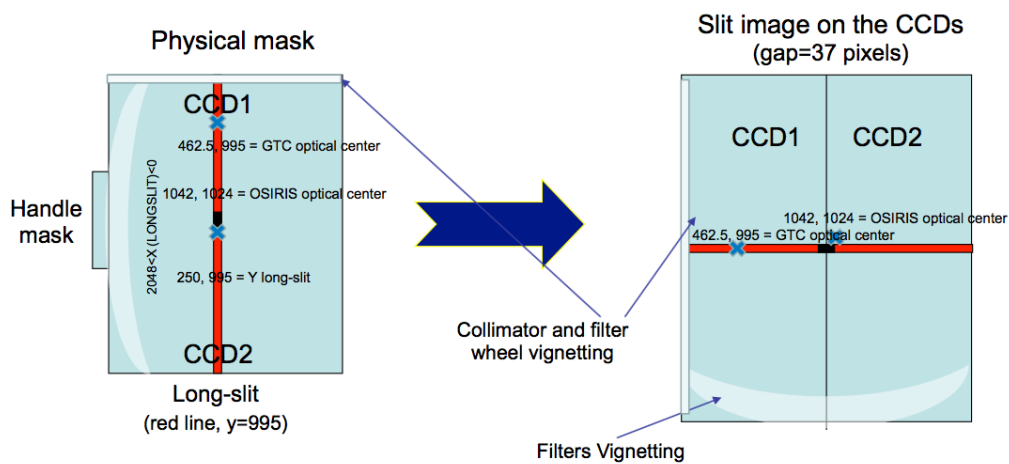
Figure 28. Physical long-slit mask correspondence with the OSIRIS CCD (Credit: GTC).

components and mechanical enclosure, these will be considered in the Preliminary phase of the design that will include the study of tolerances.

The MAAT space envelope and interfaces presented and discussed in Section 4.2 have been closely taken into consideration to make sure that the entire optical system and their components will fit well into the available space. As mentioned above the MAAT box that contains the AIS-IFU optics will be placed into the input focal plane of
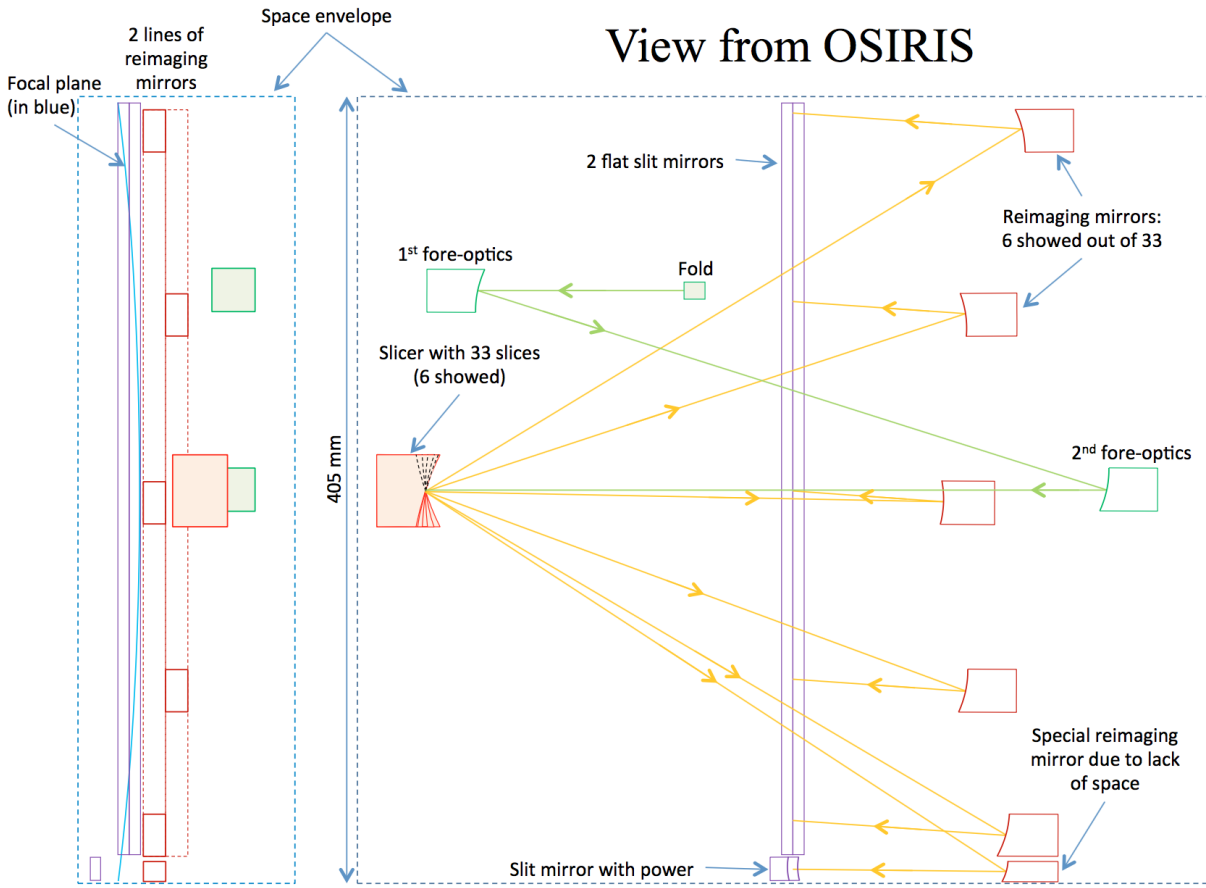
Figure 29. Optics lay-out of the proposed IFU concept (only 6 out of 33 slices are shown).

OSIRIS, as in the case of the IFU-module for the GMOS spectrograph on Gemini (Allington-Smith et al. 2000). The IFU consists of an imaging slicer optical system with 33 slices each of $0.303'' \times 14.20''$ (with 4 pixels between slice images along the slit), and a slit length of 8.0 arcmin. The spatial sampling $0.303'' \times 0.127''$ is better than the typical seeing of $0.8''$, which guarantees an appropriate sampling even with $0.303'' \times 0.254''$ by adopting an 1×2 CCD binning. The slicer width $0.303''$ yields a spectral element of 3 pixels, i.e. a resolution 1.6 times larger than the standard long-slit width of $0.6''$, as discussed in Section 4.1.

The IFU consists of a folded pick-off mirror, fore-optics, the slicing mirror array, re-imaging mirrors, and 2 flat slit mirrors. There are in total 6 reflections in the IFU system. The optics layout of the IFU system is shown in Figure 29 for only 6 slicers. The positions and sizes of the slicer, slit, and re-imaging mirrors are quite realistic. The input field pick-off mirror is fixed but it can be placed almost anywhere in the focal plane. It folds the telescope beam into the fore-optics which re-images the focal plane of the telescope on the slicing array with the proper magnification. The telescope focal plane is then divided into 33 slitlets by the slicing mirror array, similar to that shown in Figure 30. The proposed concept has similarities with that designed by Robert Content for OCTOCAM (Content et al. 2018). Each mirror in the slicer stack is tilted with a different angle so that the light is reflected in a different direction toward the re-imaging mirrors. Each beam from a slicing mirror hits a different re-imaging mirror which images the slice on the slit. All the 33 slices are then imaged side-by-side on the slit with a gap of 4 pixels (on the detector) between them to avoid cross-talks. The reflection on the 2 flat slit mirrors sends the light in the right direction into the OSIRIS spectrograph. Note that the 2 flat slit-mirrors in this drawing are incomplete, they have a more complex edge-shape than shown here. The slit beginning and end are determined by the vignetting of the collimator (as discussed in Section 4.2). In Figure 29, the distance from the slit-end to the space-envelope-edge is about 3 mm at the top and 1.5 mm at the bottom. The input beam on the slit has an angle of about $4°$ due to the tilt of the frame (as that of the OSIRIS long-slit). The *special* re-imaging mirror at the bottom does not need the beam tilt before its powered

Table 5. IFU optical parameters

Parameter	Value
Number of slices	33
Free space between slice images along slit	0.42 mm
Slice image length on slit	11.72 mm
Slice image pitch on slit	12.14 mm
Slice width	0.8 mm
Slicer width	$0.8 \times 33 = 26.4$ mm
Slice length	37.49 mm
Focal length on slicer	544594 mm
Focal ratio on slicer	f/52.365
Slit mirror position vs slit focal plane centre (sag/2)	5.53 mm
Distance re-imaging mirror to slit focal plane (centre)	83.25 mm
Distance re-imaging mirror to slit mirror (centre)	$83.25 - 5.53 = 77.72$ mm
Distance re-imaging mirror to slicer (centre)	267.01 mm
Footprint width on re-imaging (centre)	5.27 mm
Footprint length on re-imaging (centre)	$5.27 + 11.72 = 16.99$ mm
Distance re-imaging mirror to slit mirror (top edge)	118.33 mm
Distance re-imaging mirror to slicer (top edge)	363.8 mm
Footprint width on re-imaging (top edge, parallel to slit mirror)	6.95 mm
Footprint length on re-imaging (top edge, parallel to slit mirror)	$6.95 + 11.72 = 18.67$ mm
Minimum size largest re-imaging (2mm chip zone)	22.67 mm $\times$ 10.95 mm
Pitch re-imaging on each row	$2 \times 12.14 = 24.28$ mm
Re-imaging mirror surface shape	toroidal
Typical re-imaging mirror radius of curvature (increase from centre to edge)	$\sim$150 mm
Slice mirror surface shape	spherical
Rough estimate of typical slice radius of curvature	$\sim$300 mm

slit-mirror, which is tilted accordingly. The curved focal plane (pseudo-slit) on the left panel is part a real image and part a virtual image.

We provide in Table 5 the relevant parameters for all the IFU optical elements of MAAT: slicing mirror array, re-imaging mirrors and slit. The slicing mirrors are all spherical with the same radius of curvatuture. The re-imaging mirrors are toroidal in the proposed concept. Currently we are discussing with Winlight two extreme solutions: 1) All re-imaging mirrors are spherical with the same RoC (positions of the mirrors give the focus). We expect that this would minimize cost but would degrade the performances both by increasing aberrations and changing the magnification on the detector (different slice images would have different $''/pix$ so different width, thus different spectral resolution unless the slices themselves have different widths). Worst aberrations (at the edges of the slit) should be quite large; 2) Each re-imaging mirror is toroidal with the values of the radii and direction of the toroid different from the others, so there would be $2 \times 33 = 66$ different radii and 33 different directions. This would also permit to correct some of the aberrations of the spectrograph. This may increase the cost. The difference between the 2 radii of each mirror would be zero in the centre increasing roughly linearly to about 10% at the edge. The average between the 2 radii should be around 130 mm in the centre increasing parabolically to about 170 mm at the edge. The goal here is to understand
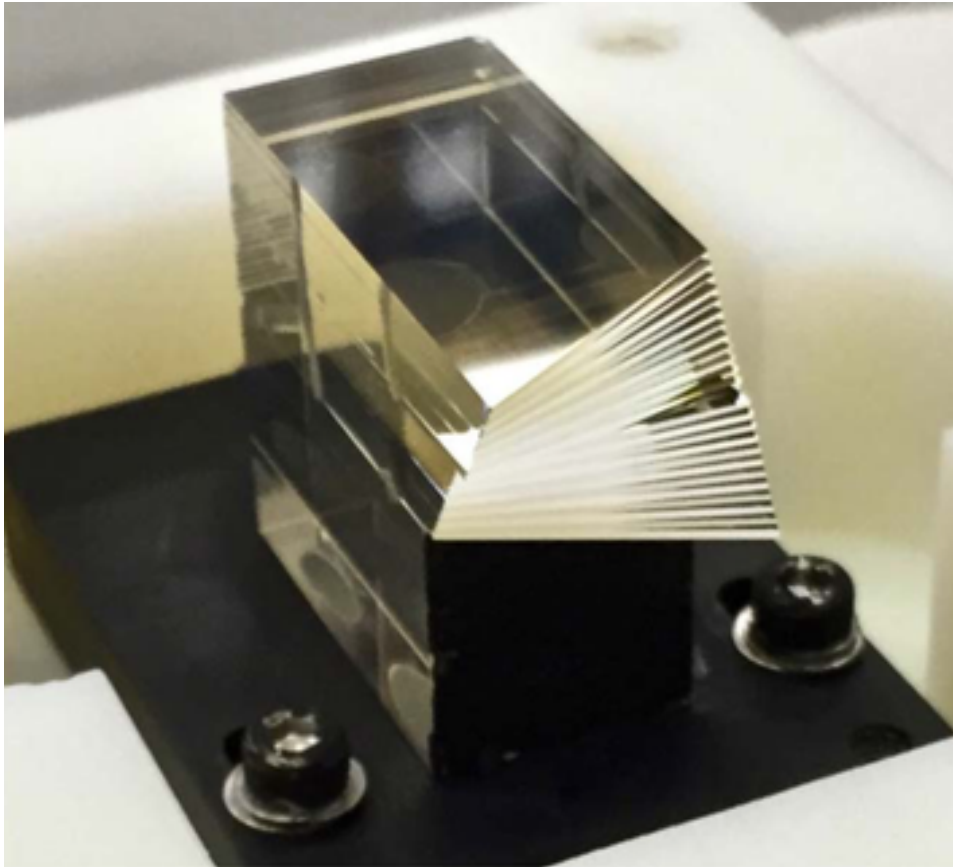
Figure 30. A close-up view of the KCWI slicer built at Winligth. This element is made from optically contacted Zerodur. Each of the 24 slitlets is 0.5 mm thick and 14.8 mm tall. The reflective faces are convex with a radius of curvature of 5206 mm, see (Morrissey et al. 2018) for more details. The MAAT slicing mirror stack will be very similar but with 33 slicers each 0.8 mm thick (see Table 5).

if having an identical shape on many mirrors does not change the costs or that it is the complexity of the shape that matters, not the number of identical mirrors. This is important because if the cost is the same for 33 spherical mirrors with different RoCs than with the same RoC, it would be a serious improvement to have them all different. Hopefully we will have very soon a detailed answer from Winlight with their trade-off study. This will help us to proceed with the current concept and start the formal Conceptual design phase. Finally, note that we have not studied in detail the fore-optics: We are considering for now a mirror optical solution. In any case it seems a feasible component from previous experience.

As seeing so far, the MAAT IFU slicer uses mirrors and hence we will require very good reflective coating for the entire spectral range $360 - 1000$ nm. Both, MUSE and KCWI have high efficiency in their slicer IFUs. The required transmission should be at least 80% on average. Currently we are using the coating spectral efficiency data provided by Winlight to compute the expected efficiency of the IFU taking into account that there are 6 reflections in the IFU (see Figure 29). This gives an average reflectivity $> 92\%$ over the whole spectral range. We should consider this a conservative value. Further investigation together with Winlight is going on to optimize the mirror coatings and increase the efficiency.

4.4. *Overall throughput and performance of OSIRIS+MAAT*

The overall efficiency of the OSIRIS+MAAT system (IFU mode including the atmosphere and the telescope) has been estimated starting from the results posted in the OSIRIS website measured from a spectrophotometric standard star through a wide slit, as a function of wavelength and for different Grisms and VPHs. The results are displayed in Figure 31 for the broadband R1000B and R1000R Grisms. We compare the expected total throughput of the OSIRIS IFU and long-lit modes on the Cassegrain with that measured at its current location on the Nasmyth focus. The gain

in sensitivity is significant below ~ 6000 Å, with a $\sim 50\%$ enhancement in the blue domain $\sim 3700 - 5000$ Å, due mostly to the new e2v detector and the absence of M3.
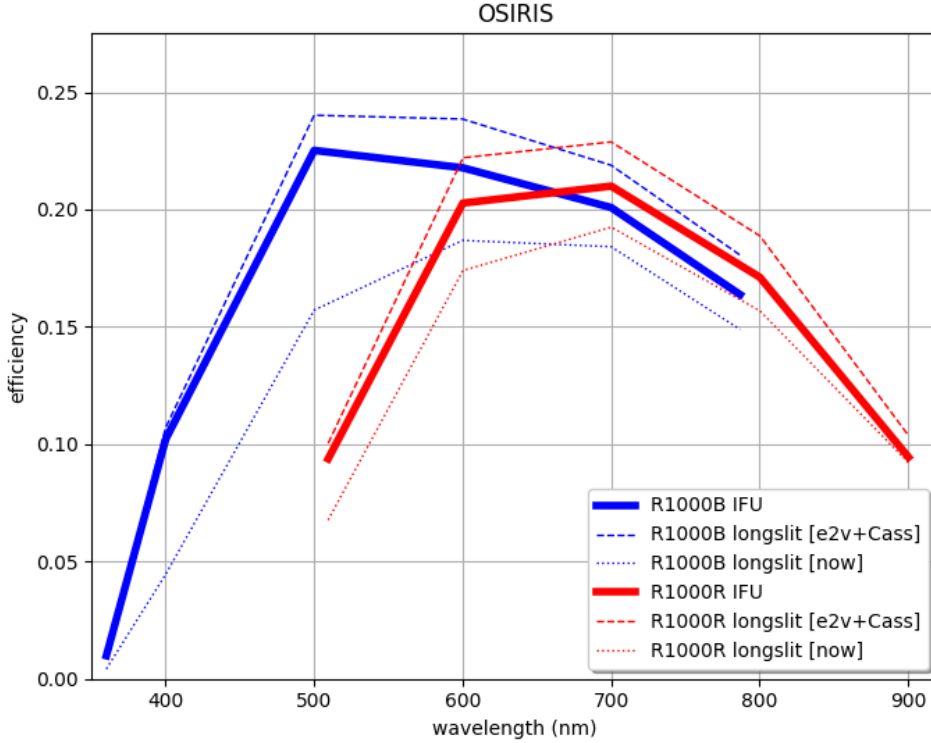
Figure 31. Total throughput (atmosphere, telescope, and instrument) of the OSIRIS long-slit and IFU mode as currently mounted on the Nasmyth focus and as it will be on the Cassegrain, which will result in a significant gain in efficiency derived from the new e2v detector and the absence of M3. The curves are shown for the broadband R1000B and R1000R Grisms.

We have used the expected efficiency curve of OSIRIS+MAAT and the OSIRIS long-slit limiting magnitudes provided in the OSIRIS website to predict the performance of the OSIRIS IFU mode for spectral continuum observations of point sources. Figure 32 shows the limiting magnitudes (AB) to reach $S/N = 5$ in 1 h of integration time with OSIRIS+MAAT for the broadband R1000B and R1000R (assuming $1''$ seeing, dark night, and airmass $= 1.2$). Note that these estimates can be obtained for any of the OSIRIS Grisms and VPHs.

In order to estimate the MAAT limiting flux we have used the MUSE@VLT exposure time calculator with the following assumptions to achieve a $S/N = 5$ with 30 exposures of 1800s each: an extended Lyα emitting galaxy with a Sersic profile at redshift ~ 4, a peak emission line flux of 3×10^{-18} erg s^{-1} cm^{-2} arcsec^{-2} (Wisotzki et al. 2018), a line width of 600 km s^{-1}, spatial binning of 3×3 and integrated over the spectral line profile, seeing of $0.8''$, dark moon, and PWV=5 mmH2O.

We want to remark that a clear advantage of IFS as compared to long-slit is the fact that all the flux of the object (point sources or extended features inside the IFU F.o.V) can be collected (see Figure 33), and hence enhancing the measured S/N and allowing to perform absolute spectro-photometry.

5. DATA SIMULATIONS AND PIPELINE OVERVIEW

We have carried out simulations to have an overview of the data reduction process. For this purpose we use MUSE@VLT data cubes as proxies for real targets on sky and then transform them through the instrumental specifications of OSIRIS+MAAT adopting the R1000R Grism to produce raw detector spectral images. The main limitation of this process is that MUSE@VLT does not provide information bluewards of 4750 Å.
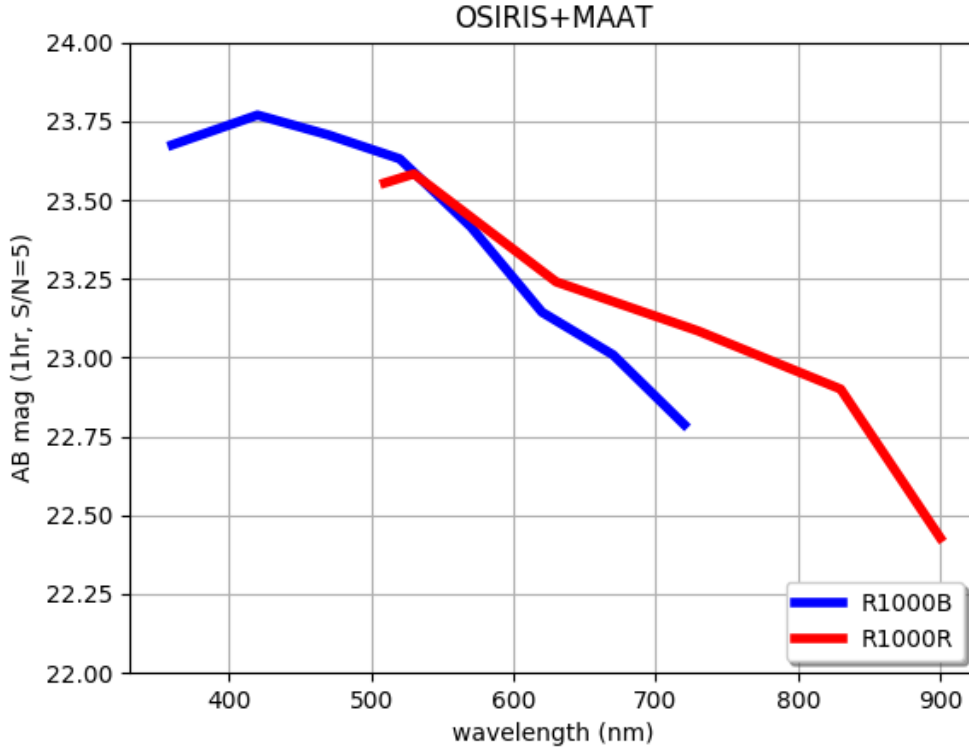
Figure 32. OSIRIS+MAAT limiting magnitudes for the broadband R1000B and R1000R Grisms.

We illustrate the process with four extragalactic astronomical targets: (i) the kilonova GRB170817A in NGC4993 as an example of time domain EM-GW counterpart and a point source, (ii) the galaxy IIZw40 as an example of a young low metallicity galaxy circumnuclear region, and two individual objects in the galaxy NGC300: (iii) the giant HII region De74 and (iv) the SNR S14. These last two cases are already showcased above (§1).

The top-left of Figure 34 shows an image of the galaxy NGC4993 with the kilonova framed by a box of $14.2'' \times 10''$ corresponding to the MAAT FoV. On the right, the kilonova as viewed by MAAT, with 33 slices of $0.303''$ each in the vertical axis and $14''$ of $0.254''$ pixels in the horizontal axis. This input image is then dispersed by the slicer and re-imaged onto the CCD detector. This CCD spectral image is shown in the bottom, where the spectral direction is along the vertical axis and the spatial-slicer direction along the horizontal axis. (Notice that due to the limited blue cutoff of MUSE@VLT these simulations stop at 4750 Å) In the spatial-slicer direction slice #1, corresponding to the bottom of the image above, is located on the left end of the CCD, and all the slices follow to the right, each separated by 4 CCD pixels from the previous slice, so that the top slice in the image above is placed on the far right end of the horizontal axis in the CCD. This can be clearly followed in this field because the bulge of NGC4993, seen in the bottom right side of the FoV, is spectrally detected in the left slices of the CCD frame (thin blue lines), while the spectrum of the kilonova centered in the central slices is seen as a point source continuum in the central slices of the CCD spectral frame (thin red lines).

As in the case of the kilonova, Figure 35 shows the corresponding images for the case of the low metallicity dwarf galaxy IIZw40. This case has been chosen to highlight the rich emission line spectrum.

The bottom images in Figures 34 and 35 show a typical readout frame from the detector of OSIRIS+MAAT. This file has to go through the reduction pipeline to be calibrated in wavelength and flux and reassembled into a spectral cube fully corrected for instrumental effects.

The MAAT data processing will consist of basic processing (including bias correction, flat-fielding, and geometrical corrections) and post-processing, including wavelength and flux calibration and sky subtraction. The FITS header from OSIRIS+MAAT will not require any new field; it will suffice to give appropriate values to the standard fields:
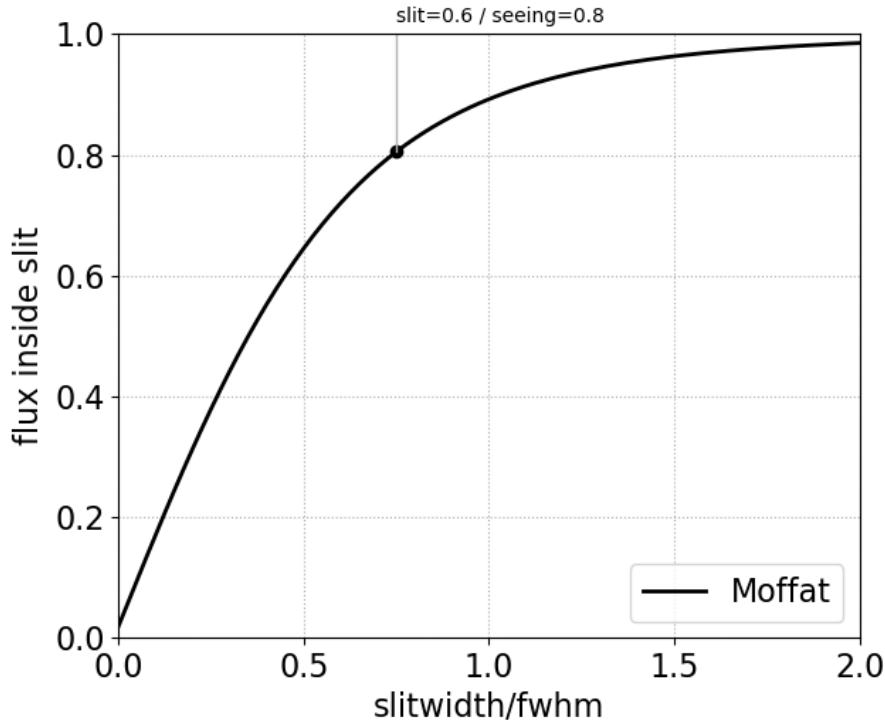
Figure 33. Flux inside the slit vs. the slit-width to seeing (fwhm) ratio adopting a Moffatt PSF. For a typical seeing of $0.8''$ one expects an increased of 20% in the total flux when the observation is done with OSIRIS+MAAT as compared to the standard OSIRIS $0.6''$ long-slit.

- "MASKNAME= 'MAAT' / Multi-object mask name"

- "OBSMODE = 'OsirisMAATspectroscopy' / Observation Mode".

We will also provide a *quick-look* pipeline with basic functions to be used by the Support Astronomers during the observing runs.

Add here a half page with more details on the data reduction pipeline.

6. OBSERVING WITH OSIRIS+MAAT

We propose that the MAAT module be permanently mounted on the OSIRIS Cartridge from late 2021 onwards, thereby enabling immediate response to transient targets and the execution of standard programs at any given time. Yet, it can be removed from the Cartridge as any other OSIRIS mask if necessary since it uses the same mask-frame interface.

MAAT can be easily used by the GTC Support Astronomers via the OSIRIS control software by selecting the appropriate mask position of the Cartridge where it is inserted. MAAT does not require from GTC staff any daily nor night technical engineering support or specific telescope operation.

Overall, the observation procedure with MAAT is simple. To ensure accurate acquisition and centering the telescope must be pointed to the center of the IFU pick-off mirror (see Figure 29). This position is accurately known with respect to both the OSIRIS and telescope optical-axis positions. The $1''$ r.m.s. pointing error of GTC guarantees that the target will be placed right at the very center of the IFU F.o.V. The same acquisition procedure applied for MEGARA and EMIR MOS can be applied to MAAT, which will guarantee a target positioning better than $0.3''$ (a spaxel). Note that the main advantage of MAAT is that a broad-band image of the entire $10'' \times 14.2''$ field could be generated from the 3D data cube, which will confirm the correct target acquisition, but at the same time will guarantee observations, and spectra, of targets whose position is known within an accuracy of few arcsecs. This represents another advantage to use MAAT, in particular for transient astrophysics. Focusing optimisation should be done even if one starts from a
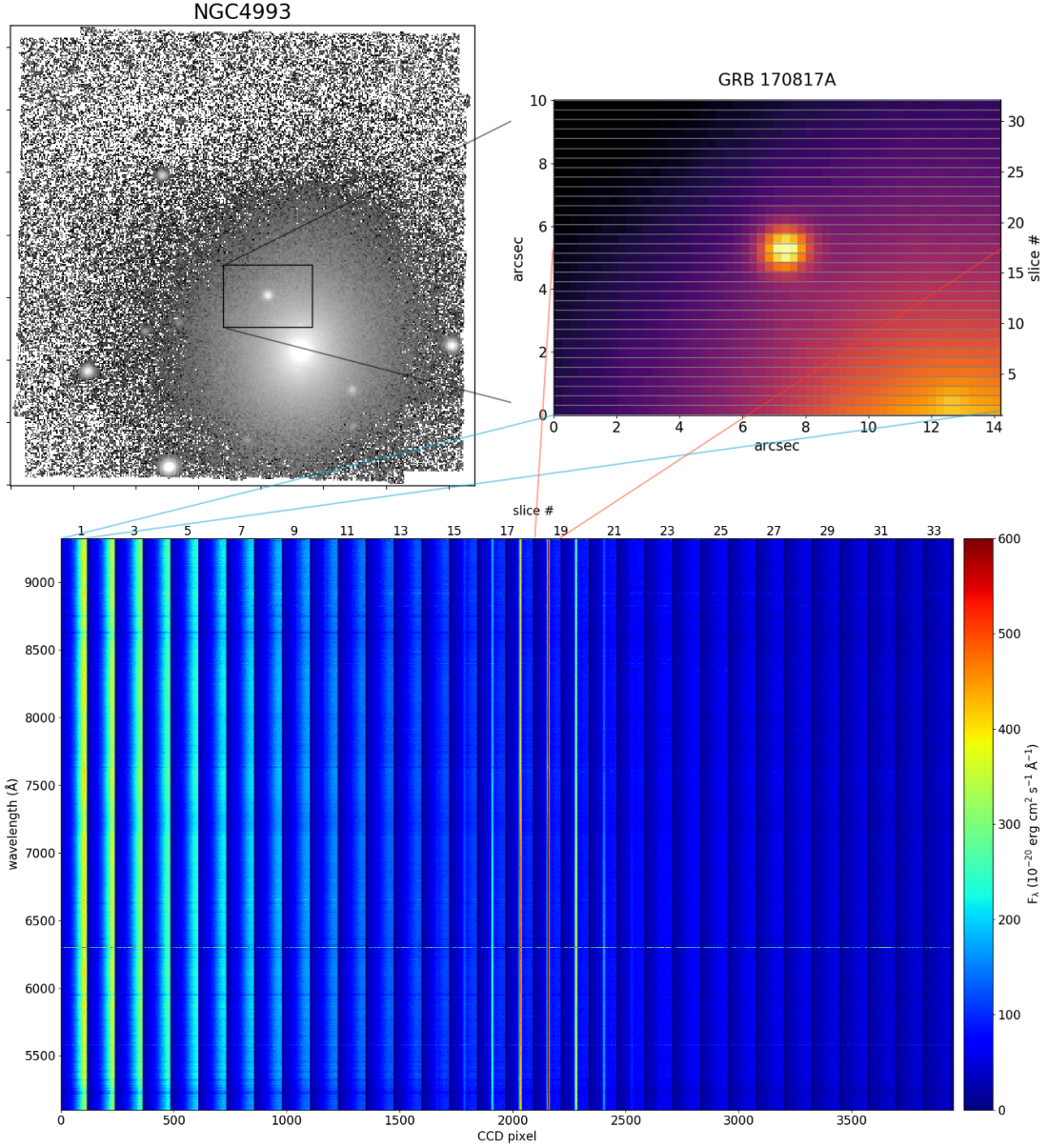
Figure 34. MAAT simulation of the kilonova GRB170817A in NGC4993.

previous OSIRIS long-slit focus, but with the advantage that the slicer gives much more information than a long-slit, thanks to its imaging capability, thus a better focusing is possible. The Instrument Calibration Module at GTC with the three different calibration lamps (HgAr, Ne, and Xe) will be used to obtain the arc lines for the selected OSIRIS Grisms and VPHs. Any other calibration frames such as dark, bias, and flat-fields will be also necessary. MAAT generates similar data rates than any other typical OSIRIS long-slit observing runs. The FITS header from OSIRIS+MAAT will not require any new field; it will suffice to give appropriate values to the standard fields (see Section 5).

The MAAT team will provide an on-line user-manual with detailed observing and calibration procedures, and guidelines for the public available data reduction pipeline. A quick-look pipeline will also be provided to assist the Support Astronomers during the observing runs, which will include acquisition and focusing scripts.

Our observing requirements for the science programs described in Section 3 requires both rapid response to transient events as well as standard observations.
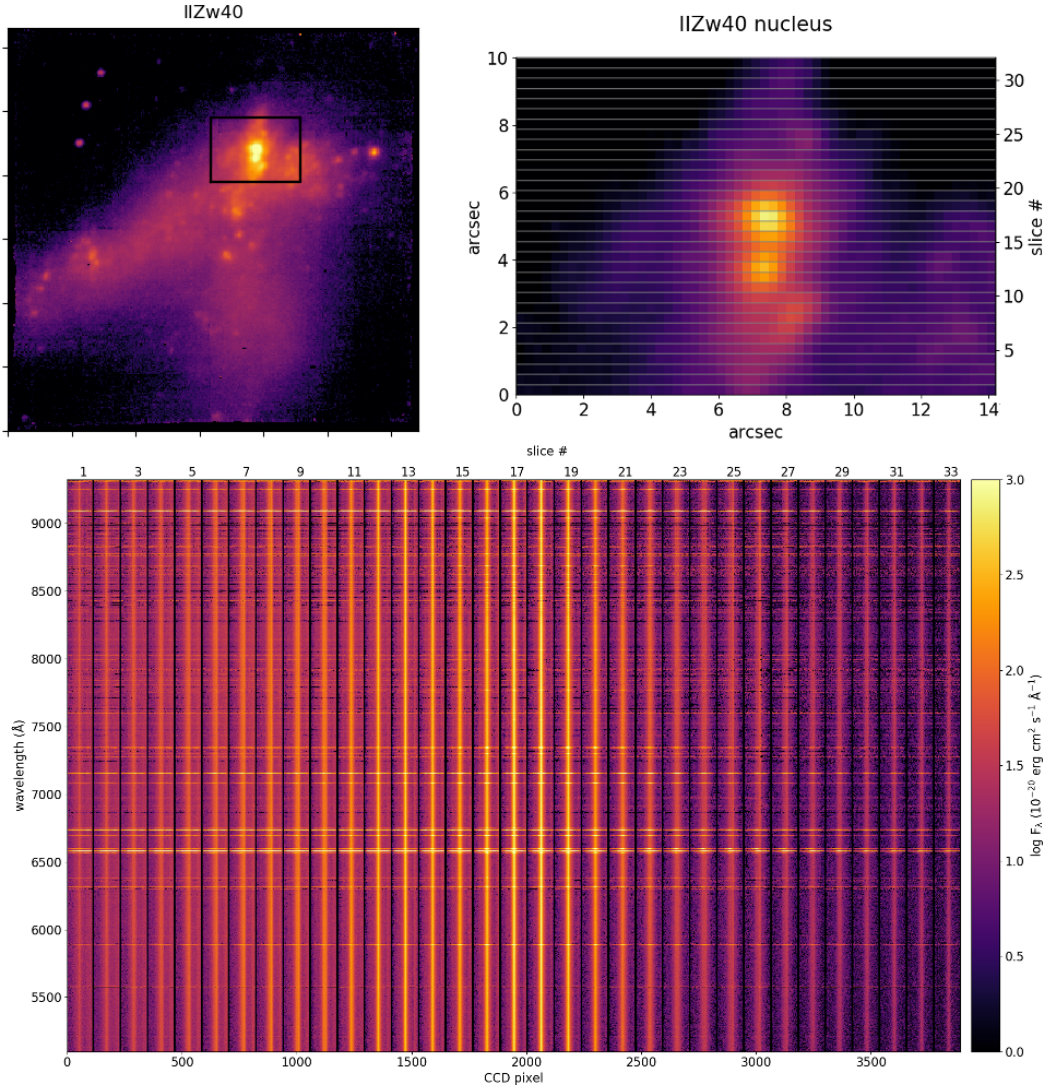
Figure 35. MAAT simulation of the circumnuclear region in the low metallicity dwarf galaxy IIZw40.

7. REMARKS AND ACKNOWLEDGEMENTS

This MAAT@GTC White Paper has fulfilled the goals of presenting the different aspects of the project and to collect outstanding science cases that justify its need and the interest of the GTC community, whom had the opportunity to attend the "Panoptic spectroscopy of our universe with OSIRIS+MAAT at GTC" workshop on May 5, 2020, to encourage and support the development of this new facility. Slides and videos of the workshop presentations can be found at the workshop website[8]. A MAAT@GTC Proposal has been already submitted to the GTC Office for its consideration.

The MAAT@GTC Collaboration consists of a group of scientists and engineers in Spain (Centro de Astrobiología CSIC-INTA, Departamento de Física Fundamental Universidad de Salamanca, Departamento de Física Teórica y del Cosmos Universidad de Granada, Instituto de Astrofísica de Andalucía CSIC, Instituto de Astrofísica de Canarias, Instituto de Física de Cantabria CSIC-UC), Australia (Australian Astronomical Optics - Macquarie University), Denmark (DARK, Neils Bohr Institute), and Sweden (The Oskar Klein Centre for Cosmoparticle Physics, Stockholm University) led by Francisco Prada as MAAT Principal Investigator. We shall strive to integrate in the MAAT team other scientists and institutions from the GTC user community interested in this mission.

REFERENCES

Abbott, B. P., Abbott, R., Abbott, T. D., & Acernese, F. e. a. 2017a, Nature, 551, 85, doi: 10.1038/nature24471

—. 2017b, Nature, 551, 85, doi: 10.1038/nature24471

Aldering, G., Adam, G., Antilogus, P., et al. 2002, in Society of Photo-Optical Instrumentation Engineers (SPIE) Conference Series, Vol. 4836, SPIE, ed. J. A. Tyson & S. Wolff, 61–72, doi: 10.1117/12.458107

Allington-Smith, J. R., Content, R., Dodsworth, G. N., et al. 2000, Society of Photo-Optical Instrumentation Engineers (SPIE) Conference Series, Vol. 4008, Integral field spectroscopy with the GEMINI multi-object spectrographs, ed. M. Iye & A. F. Moorwood, 1172–1180, doi: 10.1117/12.395436

Arcavi, I., Hosseinzadeh, G., Howell, D. A., et al. 2017, Nature, 551, 64, doi: 10.1038/nature24291

Arribas, S., Mediavilla, E., García-Lorenzo, B., del Burgo, C., & Fuensalida, J. J. 1999, A&AS, 136, 189, doi: 10.1051/aas:1999463

Arrigoni Battaia, F., Prochaska, J. X., Hennawi, J. F., et al. 2018, MNRAS, 473, 3907, doi: 10.1093/mnras/stx2465

Bailey, J. 1998, MNRAS, 301, 161, doi: 10.1046/j.1365-8711.1998.02010.x

Baines, D., Oudmaijer, R. D., Mora, A., et al. 2004, MNRAS, 353, 697, doi: 10.1111/j.1365-2966.2004.08104.x

Bergamini, P., Rosati, P., Mercurio, A., et al. 2019, A&A, 631, A130, doi: 10.1051/0004-6361/201935974

Betoule, M., Kessler, R., Guy, J., et al. 2014, A&A, 568, A22, doi: 10.1051/0004-6361/201423413

Birrer, S., Refregier, A., & Amara, A. 2018, ApJL, 852, L14, doi: 10.3847/2041-8213/aaa1de

Birrer, S., Treu, T., Rusu, C. E., et al. 2019, MNRAS, 484, 4726, doi: 10.1093/mnras/stz200

Bonvin, V., Courbin, F., Suyu, S. H., et al. 2017, MNRAS, 465, 4914, doi: 10.1093/mnras/stw3006

Brout, D., Scolnic, D., Kessler, R., et al. 2019, ApJ, 874, 150, doi: 10.3847/1538-4357/ab08a0

Caminha, G. B., Grillo, C., Rosati, P., et al. 2017, A&A, 600, A90, doi: 10.1051/0004-6361/201629297

Caminha, G. B., Rosati, P., Grillo, C., et al. 2019, A&A, 632, A36, doi: 10.1051/0004-6361/201935454

Cid Fernandes, R., Pérez, E., García Benito, R., et al. 2013, A&A, 557, A86, doi: 10.1051/0004-6361/201220616

Content, R. 1998, Society of Photo-Optical Instrumentation Engineers (SPIE) Conference Series, Vol. 3354, Advanced image slicers for integral field spectroscopy with UKIRT and GEMINI, ed. A. M. Fowler, 187–200, doi: 10.1117/12.317262

—. 2000, Astronomical Society of the Pacific Conference Series, Vol. 195, Advanced Image Slicers from the Laboratory to NGST, ed. W. van Breugel & J. Bland-Hawthorn, 518

—. 2006, Society of Photo-Optical Instrumentation Engineers (SPIE) Conference Series, Vol. 6269, Optical design of the KMOS slicer system, 62693S, doi: 10.1117/12.672312

Content, R., de Ugarte Postigo, A., Thöne, C., & Sheinis, A. 2018, in Society of Photo-Optical Instrumentation Engineers (SPIE) Conference Series, Vol. 10706, Proc. SPIE, 107066L, doi: 10.1117/12.2314424

Corradi, R. L. M., García-Rojas, J., Jones, D., & Rodríguez-Gil, P. 2015, ApJ, 803, 99. https://arxiv.org/abs/1502.05182

D'Andrea, C. B., Gupta, R. R., Sako, M., et al. 2011, ApJ, 743, 172, doi: 10.1088/0004-637X/743/2/172

Dhawan, S., Johansson, J., Goobar, A., et al. 2019, MNRAS, 2578, doi: 10.1093/mnras/stz2965

Diego, J. M., Kaiser, N., Broadhurst, T., et al. 2018, ApJ, 857, 25, doi: 10.3847/1538-4357/aab617

Eldridge, J. J., Stanway, E. R., Xiao, L., et al. 2017, PASA, 34, e058, doi: 10.1017/pasa.2017.51

Freedman, W. L., Madore, B. F., Hatt, D., et al. 2019, ApJ, 882, 34, doi: 10.3847/1538-4357/ab2f73

Galbany, L., Stanishev, V., Mourão, A. M., et al. 2014, A&A, 572, A38, doi: 10.1051/0004-6361/201424717

—. 2016a, A&A, 591, A48, doi: 10.1051/0004-6361/201528045

Galbany, L., Anderson, J. P., Rosales-Ortega, F. F., et al. 2016b, MNRAS, 455, 4087, doi: 10.1093/mnras/stv2620

Galbany, L., Anderson, J. P., Sánchez, S. F., et al. 2018, ApJ, 855, 107, doi: 10.3847/1538-4357/aaaf20

García-Rojas, J., Corradi, R. L. M., Monteiro, H., et al. 2016, ApJL, 824, L27. https://arxiv.org/abs/1606.02830

García-Rojas, J., Wesson, R., Boffin, H. M. J., et al. 2019, arXiv e-prints, arXiv:1904.06763. https://arxiv.org/abs/1904.06763

Gnerucci, A., Marconi, A., Capetti, A., Axon, D. J., & Robinson, A. 2010, A&A, 511, A19, doi: 10.1051/0004-6361/200912530

Gnerucci, A., Marconi, A., Capetti, A., et al. 2011a, A&A, 536, A86, doi: 10.1051/0004-6361/201117388

Gnerucci, A., Marconi, A., Cresci, G., et al. 2011b, A&A, 528, A88, doi: 10.1051/0004-6361/201015465

Goldstein, A., Veres, P., Burns, E., et al. 2017, ApJL, 848, L14, doi: 10.3847/2041-8213/aa8f41

Goldstein, D. A., Nugent, P. E., & Goobar, A. 2019, ApJS, 243, 6, doi: 10.3847/1538-4365/ab1fe0

Gómez-Llanos, V., Morisset, C., García-Rojas, J., et al. 2020, submitted to ApJL

Goobar, A., Amanullah, R., Kulkarni, S. R., et al. 2017, Science, 356, 291, doi: 10.1126/science.aal2729

Grillo, C., Lombardi, M., Rosati, P., et al. 2008, A&A, 486, 45, doi: 10.1051/0004-6361:200809434

Grillo, C., Rosati, P., Suyu, S. H., et al. 2018, ApJ, 860, 94, doi: 10.3847/1538-4357/aac2c9

Gupta, R. R., D'Andrea, C. B., Sako, M., et al. 2011, ApJ, 740, 92, doi: 10.1088/0004-637X/740/2/92

Gustafsson, B. 1992, in European Southern Observatory Conference and Workshop Proceedings, Vol. 40, European Southern Observatory Conference and Workshop Proceedings, 17

Hamuy, M., Trager, S. C., Pinto, P. A., et al. 2000, AJ, 120, 1479, doi: 10.1086/301527

Henault, F., Bacon, R., Content, R., et al. 2004, Society of Photo-Optical Instrumentation Engineers (SPIE) Conference Series, Vol. 5249, Slicing the universe at affordable cost: the quest for the MUSE image slicer, ed. L. Mazuray, P. J. Rogers, & R. Wartmann, 134–145, doi: 10.1117/12.512397

Hjorth, J., Levan, A. J., Tanvir, N. R., et al. 2017, ApJL, 848, L31, doi: 10.3847/2041-8213/aa9110

Izzo, L., Thöne, C. C., Schulze, S., et al. 2017, MNRAS, 472, 4480, doi: 10.1093/mnras/stx2244

Jee, I., Komatsu, E., & Suyu, S. H. 2015, JCAP, 2015, 033, doi: 10.1088/1475-7516/2015/11/033

Johansson, J., Goobar, A., Price, S. H., et al. 2020, arXiv e-prints, arXiv:2004.10164. https://arxiv.org/abs/2004.10164

Jones, D., Wesson, R., García-Rojas, J., Corradi, R. L. M., & Boffin, H. M. J. 2016, MNRAS, 455, 3263. https://arxiv.org/abs/1510.07516

Jones, D. O., French, K. D., Agnello, A., et al. 2019, The Astronomer's Telegram, 13330, 1

Kelly, P. L., Hicken, M., Burke, D. L., Mand el, K. S., & Kirshner, R. P. 2010, ApJ, 715, 743, doi: 10.1088/0004-637X/715/2/743

Kelly, P. L., Rodney, S. A., Treu, T., et al. 2015, Science, 347, 1123, doi: 10.1126/science.aaa3350

Kelly, P. L., Diego, J. M., Rodney, S., et al. 2018, Nature Astronomy, 2, 334, doi: 10.1038/s41550-018-0430-3

Kuncarayakti, H., Doi, M., Aldering, G., et al. 2013a, AJ, 146, 30, doi: 10.1088/0004-6256/146/2/30

—. 2013b, AJ, 146, 31, doi: 10.1088/0004-6256/146/2/31

Lampeitl, H., Smith, M., Nichol, R. C., et al. 2010, ApJ, 722, 566, doi: 10.1088/0004-637X/722/1/566

Lasker, J., Kessler, R., Scolnic, D., et al. 2019, MNRAS, 485, 5329, doi: 10.1093/mnras/stz619

Lelli, F., Verheijen, M., Fraternali, F., & Sancisi, R. 2012, A&A, 537, A72, doi: 10.1051/0004-6361/201117867

Levan, A. J., Lyman, J. D., Tanvir, N. R., et al. 2017, ApJL, 848, L28, doi: 10.3847/2041-8213/aa905f

Liu, X. W., Storey, P. J., Barlow, M. J., et al. 2000, MNRAS, 312, 585

Moreno-Raya, M. E., Galbany, L., López-Sánchez, Á. R., et al. 2018, MNRAS, 476, 307, doi: 10.1093/mnras/sty185

Moreno-Raya, M. E., López-Sánchez, Á. R., Mollá, M., et al. 2016, MNRAS, 462, 1281, doi: 10.1093/mnras/stw1706

Morrissey, P., Matuszewski, M., Martin, D. C., et al. 2018, ApJ, 864, 93, doi: 10.3847/1538-4357/aad597

Mörtsell, E., Johansson, J., Dhawan, S., et al. 2019, arXiv e-prints, arXiv:1907.06609. https://arxiv.org/abs/1907.06609

Munari, U., & Zwitter, T. 1997, A&A, 318, 269

Oguri, M., Keeton, C. R., & Dalal, N. 2005, MNRAS, 364, 1451, doi: 10.1111/j.1365-2966.2005.09697.x

Osterbrock, D. E., & Ferland, G. J. 2006, Astrophysics of gaseous nebulae and active galactic nuclei

Paraficz, D., & Hjorth, J. 2009, A&A, 507, L49, doi: 10.1051/0004-6361/200913307

Perlmutter, S., Pennypacker, C. R., Goldhaber, G., et al. 1995, ApJL, 440, L41, doi: 10.1086/187756

Perlmutter, S., Aldering, G., Goldhaber, G., et al. 1999, ApJ, 517, 565, doi: 10.1086/307221

Phillips, M. M. 1993a, ApJL, 413, L105, doi: 10.1086/186970

—. 1993b, ApJL, 413, L105, doi: 10.1086/186970

Phillips, M. M., Simon, J. D., Morrell, N., et al. 2013, ApJ, 779, 38, doi: 10.1088/0004-637X/779/1/38

Pian, E., D'Avanzo, P., Benetti, S., et al. 2017, Nature, 551, 67, doi: 10.1038/nature24298

Rebassa-Mansergas, A., Toonen, S., Korol, V., & Torres, S. 2019, MNRAS, 482, 3656, doi: 10.1093/mnras/sty2965

Refsdal, S. 1964, MNRAS, 128, 307, doi: 10.1093/mnras/128.4.307

Reindl, N., Schaffenroth, V., Geier, S., et al. 2019, in Compact White Dwarf Binaries, ed. G. H. Tovmassian & B. T. Gansicke, 7

Riess, A. G., Casertano, S., Yuan, W., Macri, L. M., & Scolnic, D. 2019, ApJ, 876, 85, doi: 10.3847/1538-4357/ab1422

Riess, A. G., Press, W. H., & Kirshner, R. P. 1996, ApJ, 473, 88, doi: 10.1086/178129

Riess, A. G., Kirshner, R. P., Schmidt, B. P., et al. 1999, AJ, 117, 707, doi: 10.1086/300738

Rigault, M., Copin, Y., Aldering, G., et al. 2013, A&A, 560, A66, doi: 10.1051/0004-6361/201322104

Rigault, M., Brinnel, V., Aldering, G., et al. 2018, arXiv e-prints, arXiv:1806.03849. https://arxiv.org/abs/1806.03849

Roman, M., Hardin, D., Betoule, M., et al. 2018, A&A, 615, A68, doi: 10.1051/0004-6361/201731425

Sánchez Almeida, J., Elmegreen, B. G., Muñoz-Tuñón, C., & Elmegreen, D. M. 2014, A&A Rv, 22, 71, doi: 10.1007/s00159-014-0071-1

Santander-García, M., Rodríguez-Gil, P., Corradi, R. L. M., et al. 2015, Nature, 519, 63, doi: 10.1038/nature14124

Schmoll, J., Dodsworth, G. N., Content, R., & Allington-Smith, J. R. 2004, Society of Photo-Optical Instrumentation Engineers (SPIE) Conference Series, Vol. 5492, Design and construction of the IMACS-IFU: a 2000-element integral field unit, ed. A. F. M. Moorwood & M. Iye, 624–633, doi: 10.1117/12.549803

Scolnic, D. M., Jones, D. O., Rest, A., et al. 2018, ApJ, 859, 101, doi: 10.3847/1538-4357/aab9bb

Shajib, A. J., Treu, T., & Agnello, A. 2018, MNRAS, 473, 210, doi: 10.1093/mnras/stx2302

Shajib, A. J., Birrer, S., Treu, T., et al. 2019, arXiv e-prints, arXiv:1910.06306. https://arxiv.org/abs/1910.06306

Shen, Y. 2012, ApJ, 757, 152, doi: 10.1088/0004-637X/757/2/152

Smartt, S. J., Chen, T. W., Jerkstrand, A., et al. 2017, Nature, 551, 75, doi: 10.1038/nature24303

Smith, M., Nichol, R. C., Dilday, B., et al. 2012, ApJ, 755, 61, doi: 10.1088/0004-637X/755/1/61

Stanishev, V., Rodrigues, M., Mourão, A., & Flores, H. 2012, A&A, 545, A58, doi: 10.1051/0004-6361/201219188

Sullivan, M., Conley, A., Howell, D. A., et al. 2010, MNRAS, 406, 782, doi: 10.1111/j.1365-2966.2010.16731.x

Takami, M., Bailey, J., & Chrysostomou, A. 2003, A&A, 397, 675, doi: 10.1051/0004-6361:20021544

Torres, M. A. P., Casares, J., Jiménez-Ibarra, F., et al. 2020, ApJL, 893, L37, doi: 10.3847/2041-8213/ab863a

Treu, T. 2010, ARA&A, 48, 87, doi: 10.1146/annurev-astro-081309-130924

Unwin, S. C., Shao, M., Tanner, A. M., et al. 2008, PASP, 120, 38, doi: 10.1086/525059

Watson, D., Hansen, C. J., Selsing, J., et al. 2019, Nature, 574, 497, doi: 10.1038/s41586-019-1676-3

Wesson, R., Jones, D., García-Rojas, J., Boffin, H. M. J., & Corradi, R. L. M. 2018, MNRAS, 480, 4589. https://arxiv.org/abs/1807.09272

Whelan, E. T., Ray, T. P., Bacciotti, F., et al. 2005, Nature, 435, 652, doi: 10.1038/nature03598

Wiseman, P., Smith, M., Childress, M., et al. 2020, MNRAS, doi: 10.1093/mnras/staa1302

Wisotzki, L., Bacon, R., Brinchmann, J., et al. 2018, Nature, 562, 229, doi: 10.1038/s41586-018-0564-6

Wyse, A. B. 1942, ApJ, 95, 356

Yao, Y., Miller, A. A., Kulkarni, S. R., et al. 2019, ApJ, 886, 152, doi: 10.3847/1538-4357/ab4cf5